J. Fluid Mech. (1999), *vol.* 399, *pp.* 205–236. Printed in the United Kingdom

Flow regimes in a wide 'sliced-cylinder' model of homogeneous beta-plane circulation

By ROSS W. GRIFFITHS AND ANDREW E. KISS

Research School of Earth Sciences, The Australian National University,
Canberra 0200 ACT, Australia

(Received 21 November 1997 and in revised form 23 January 1999)

We report new experiments with the 'sliced-cylinder' β-plane model of Pedlosky & Greenspan (1967) and Beardsley (1969), but with a much wider basin such that the western boundary current and its eddies occupy a small fraction of the basin width. These experiments provide new insights into nonlinear aspects of the flow: the critical conditions for boundary current separation and the transition from stable to unstable flow are redefined, and a further transition from periodic to chaotic eddy shedding under strong anticyclonic forcing is also found. In the nonlinear regimes the western boundary current separates from the western wall and shoots into the interior as a narrow jet that undergoes a rapid adjustment to join with the broad slow interior flow. In the unstable regimes this adjustment involves eddy shedding. Each transition occurs at a fixed critical value of a Reynolds number Re_γ based on the velocity and width scales for a purely viscous boundary current: the flow is unstable for $Re_\gamma > 123 \pm 4$ and aperiodic for $Re_\gamma > 231 \pm 5$. The results provide evidence that the mechanism causing instability is shear in the separated jet rather than the breaking of a large-amplitude Rossby wave. A quasi-geostrophic numerical model applied to the laboratory conditions yields a stability boundary and detailed characteristics of the flow largely consistent with those determined from the experiments. It also reveals a strong dependence of the circulation pattern on basin aspect ratio, and shows that an adverse higher-order pressure gradient is responsible for western boundary current separation in this model. Eddy–eddy interactions and feedback of fluctuations from the eddy formation region to upstream parts of the boundary current contribute to aperiodic behaviour. As a result of eddy shedding, passive tracer from each streamline in the boundary current can be stirred across much of the width of the basin.

1. Introduction

Simple models have played an important role in developing the understanding of midlatitude wind-driven circulation, with its intense western boundary currents, separation from the western boundary and instability in the energetic extension stream. Many of these have been barotropic models of flow on a β-plane in rectangular basins of constant depth forced by simple prescribed wind stress distributions, most often with regions of both cyclonic and anticyclonic wind stress curl. They have been used in investigations of nonlinear effects on the circulation at finite Rossby or Reynolds numbers at midlatitude (eg. Bryan 1963; Böning 1986; Ierley 1990; Kamenkovitch *et al.* 1995) and of the influence of the choice of boundary conditions (Böning 1986; Haidvogel, McWilliams & Gent 1992; Dengg 1993). They have also been used to study western boundary current separation in both viscous and conservative cases

(Veronis 1973; Pedlosky 1987; Cessi 1991; Verron & Le Provost 1991; Haidvogel *et al.* 1992; Dengg 1993), the stability of the boundary current (Ierley & Young 1991; Kamenkovitch *et al.* 1995; Sheremet, Kamenkovitch & Pastushkov 1995) and the presence of an inertial recirculating gyre in the northwest of the subtropical gyre (Bryan 1963; Kamenkovitch *et al.* 1995).

Among the results of the numerical studies we note in particular that there is a critical Reynolds number (for a given value of the Ekman number) above which the steady solution gives way to an unstable flow in which eddies are generated and an intense recirculating gyre in the northwest is also present (Bryan 1963). In recent studies using a two-gyre model that takes into account nonlinearity and lateral friction, but not bottom friction, Kamenkovitch *et al.* (1995) and Sheremet *et al.* (1995) found a second critical value of a Reynolds number (which they based on a slow interior velocity scale and the width of a purely inertial boundary layer). Above this larger critical value the boundary layer solution ceased to exist and the numerical solution became more chaotic in both the interior and boundary current. Meacham & Berloff (1997) found corresponding transitions from steady to periodic and from periodic to aperiodic for a single-gyre model.

A simple laboratory model of homogeneous ocean circulation at midlatitudes was proposed by Pedlosky & Greenspan (1967). In their 'sliced cylinder' model, flow in a rotating cylindrical basin was forced by a surface stress τ imposed by a differentially rotating lid in contact with the water and rotating at a speed $\Delta\Omega$ relative to the basin. The forcing therefore represented a uniform wind stress curl. The effects of the variation of Coriolis parameter f with latitude were modelled by imposing a variation of water depth H using a planar sloping base, such that contours of potential vorticity f/H were parallel straight lines across the basin. Thus all geostrophic contours were blocked. Beardsley (1969) investigated this model in the laboratory, and the idea has been followed up in further experimental, analytical and numerical studies (Beardsley 1973, 1975; Beardsley & Robbins 1975; Becker & Page 1990). The model reproduced the primary aspects of the mid-latitude circulation, particularly the interior Sverdrup balance closed by an intense western boundary current. For sufficiently small values of the Rossby number $\Delta\Omega/\Omega$ the observed flow was consistent with the linear analytical solution for the interior flow (Pedlosky & Greenspan 1967; Beardsley 1969), in which a balance between vortex compression (for anticyclonic forcing) due to pumping by the upper Ekman layer and stretching due to flow across the potential vorticity (depth) contours is dominant in the interior and breaks down against the western boundary to allow a return flow.

The experiments and numerical solutions for the sliced cylinder showed that for larger Rossby numbers the western boundary current intensified in the downstream direction. The outflow (in the case of anticyclonic forcing) became increasingly localized to a narrow jet accompanied by an intense anticyclonic recirculating gyre and a stationary Rossby wave-like pattern. The flow became unstable when the anticyclonic forcing was sufficiently strong. Beardsley (1969, 1973) and Beardsley & Robbins (1975) expressed the conditions for onset of instability in terms of a critical value of a Reynolds number, the value being dependent on Ekman number. They concluded that the instability was due to breaking of the large-amplitude standing Rossby wave through which the outflow stream passed. The numerical studies of Becker & Page (1990) supported an alternative instability mechanism (first suggested by Beardsley 1969) of breakdown due to strong shear in the separated jet.

The sliced-cylinder flows referred to above were clearly intensified in the west with a strong boundary current. All of the experiments and computations used 'deep' systems having width-to-height ratio, L/H, of order one. This allowed the total variation of water depth across the basin to be kept much smaller than the depth, accommodating comparison with linearized analyses at weak forcing. However, the width of the boundary current was not small compared to the width of the basin (it scales as $HE^{1/4}$ if bottom friction is the dominant dissipation – Stommel 1948; Beardsley 1969 – and as $HE^{1/3}$ if sidewall friction is dominant – Munk 1950; Munk & Carrier 1950; Beardsley 1969 – where the Ekman number E was of order 10^{-5} to 10^{-4}). Indeed, the velocity reversal between the interior Sverdrup flow and the return boundary current occurred at around one half of the cylinder radius, and the eddy structures in unstable flows filled much of the basin. Thus the previous models were not wide systems like the ocean basins, and perhaps not the most suitable for investigation of nonlinear phenomena.

In this study we examine the circulation in a wider basin where the western boundary current and its eddies fill a much smaller fraction of the basin. The role of sidewall effects other than dissipation in the western boundary current is reduced and the dependence of the flow on aspect ratio and Rossby (or Reynolds) number can be further explored. We concentrate on the case of anticyclonic forcing, or negative wind stress curl. By extending the range of conditions to strong forcing we redefine the critical conditions for instability and discover in the laboratory experiments a second transition: that from periodic to chaotic flow. This corresponds to the transition found by Kamenkovitch *et al.* (1995) in their two-gyre numerical model with no bottom friction. In order to provide further information on the flow for moderate Rossby numbers we also employ a quasi-geostrophic numerical model originally developed by Page (1982) and Becker & Page (1990). Our study of this homogeneous flow was in part motivated by an investigation, in the same apparatus, of a two-layer density-stratified flow (Griffiths & Cornillon 1994), and the present results serve to better define the barotropic flow with which the baroclinic cases can be compared. The experimental and numerical results reported here also serve as a basis of comparison for an investigation of the effects of different side boundary conditions in which we replace the vertical side boundary with a bottom slope that meets the lid around the perimeter of the basin (Griffiths & Veronis 1997, 1998).

2. Apparatus and method

The experiments were carried out in a cylindrical tank of inner diameter $L = 0.98$ m rotating about a vertical axis at an angular velocity Ω. In this tank the north-south gradient of planetary vorticity in the oceans is simulated by a linear variation of the water depth produced by planar sloping top and bottom boundaries (figure 1). The base angle α_2 from the horizontal was fixed at $\tan\alpha_2 = 0.10$. The lid angle α_1 (which is essential in two-layer experiments in order to provide a β-effect in the top layer) was adjustable and of opposite sign to the base angle. It was set to either zero or $\tan\alpha_1 = 0.05$. In the homogeneous experiments being reported here it was only the total gradient $\tan\alpha = \tan\alpha_1 + \tan\alpha_2$ of water depth that mattered, and we have $\tan\alpha = 0.10$ and 0.15. The mean depth of water, and the depth at the centre of the tank, H_0, was 12.5 cm. Hence the aspect ratio $L/H_0 = 7.84$, much larger than the aspect ratios used by Beardsley (1969, 1973) ($L/H_0 = 1.99$) and Becker & Page (1990) ($L/H_0 = 0.855$). In the following discussion we refer to directions in analogous geographic terms appropriate to a northern-hemisphere ocean basin. Thus the shallowest water in the basin is 'north' and the left-hand side of the basin when

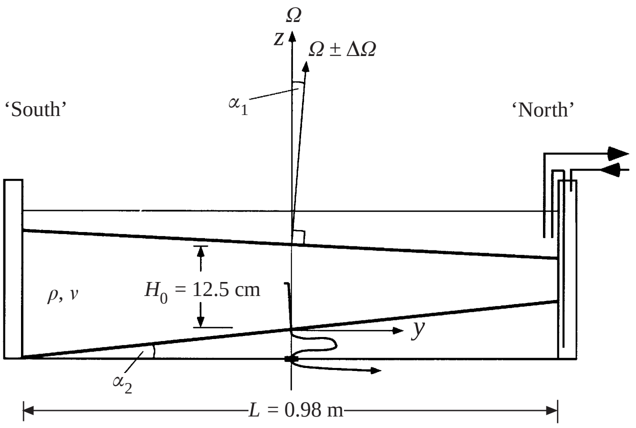

Figure 1. Diagram of the 'sliced-cylinder' apparatus with sloping base and lid, and differentially rotating lid. The working chamber, surrounding water jacket and one dye injection tube are shown as viewed from the 'east'; the x-axis points out of the page.

looking north is 'west', for this is the direction of propagation of topographic Rossby waves.

The surface stress τ applied to the water by the rotating lid is given by $\tau = \rho r \Delta\Omega(\nu\Omega)^{1/2}$, where r is the radial position and ν is the kinematic viscosity of the water. In order to avoid unwanted forcing components it was important that the lid rotate at a uniform speed, that the lower surface of the lid be planar and that it rotated true without displacements normal to its plane. In a first set of experiments the lid was a 1 cm thick Perspex sheet, chosen for its uniform thickness and flatness. However, in order to eliminate the possibility of distortions due to absorption of water in the Perspex, the lid in most experiments was a 1 cm thick float-glass plate. The lids were cut to fit within the outer wall of the cylindrical tank with a 1 mm gap and sealed against water transport by a flexible nylon-on-rubber strip fixed to the lid and sliding against the wall. The lid was supported from above by eight equally spaced legs attached close to the outer edge of the lid and connected to a rigid drive ring above the tank. The drive ring was supported by four pairs of angular-contact bearings rigidly attached to a frame which was, in turn, rigidly connected to the rotating table. The whole support assembly was pivoted about an east-west axis through the centre of the tank at the height of the lid so that the lid could be tilted to an angle from the horizontal while keeping it centred on the cylinder and rotating about its normal axis (figure 1). The lid was driven by a stepper motor via a small wheel against the outer rim of the drive ring. In order to test for any imperfections giving unwanted vertical displacements of the lids, each lid was tested with a micrometer gauge mounted inside the tank to monitor the lower surface of the lid while it rotated. Vertical displacements about the mean position were approximately ± 0.1 mm for the Perspex lid and ± 0.05 mm for the glass lid. The drive ring and bearing assembly was of a larger diameter than the tank, leaving the full area of the cylinder open to viewing from above.

The cylinder was constructed inside a larger square tank and the intervening space was filled with water to allow the flow to be observed horizontally through the sidewalls without undue distortion. This outer chamber also served as a temperature-controlled bath insulating the working chamber against heat exchange with the room. Insulation above the lid also was found to be necessary, otherwise even minor cooling produced small convective vortices throughout the slow interior flow when experiments having slow forcing were run for an hour or more. This problem was solved by covering the lid with 5–10 cm of water pumped continuously from a temperature bath in the non-rotating reference frame (and held to within $\pm 0.02\,^\circ$C), through rotating fluid couplings to the rotating table. The same water was passed through the outer chamber surrounding the cylinder. This arrangement kept the water in the working chamber at a constant temperature of $20.6 \pm 0.1\,^\circ$C despite room air-conditioning and diurnal temperature cycles.

A range of tank rotation speeds $\Omega = 0.5$–$2.0\,\mathrm{rad\,s^{-1}}$ and relative lid speeds $\Delta\Omega = 0.0051$–$0.16\,\mathrm{rad\,s^{-1}}$ (or lid periods of 1228 s to 40 s) gave Rossby numbers $Ro = \Delta\Omega/\Omega$ in the range $0.0026 < Ro < 0.16$ and Ekman numbers $E = \nu/\Omega H_0^2$ in the range $3.15 \times 10^{-5} < E < 1.26 \times 10^{-4}$, where $\nu = 0.99 \times 10^{-6}\,\mathrm{m^2\,s^{-1}}$ is the kinematic viscosity of the water. These parameters give $E^{1/4} \sim \tan\alpha$ and conditions that are predicted to place the western boundary current in a mixed regime between that of Stommel (1948) (dominated by Ekman dissipation) and that of Munk (1950) (dominated by dissipation on the sidewall) (Beardsley 1969; Beardsley & Robbins 1975). Much smaller gradients of water depth would have given boundary currents in the Stommel regime, but the westward intensification would have been much reduced. Larger slopes, on the other hand, would have given variations of water depth as large as the depth, hence a large distortion of the flow (outside regions where the Stommel and Sverdrup balances hold) due to streamtube depth changes. The chosen slope, depth and basin width therefore represent a compromise. We also note that the potential vorticity gradient is not precisely constant as a consequence of the finite relative depth variation.

A particularly effective but simple method of flow visualization in these experiments is to bleed narrow streams of neutrally buoyant dye into the flow from syringe tubes of 1.5 mm diameter positioned at strategic points in the tank. In order to match the density of the aqueous dye solutions, in most experiments a small quantity of salt was added to the water in the basin. In other experiments a small amount of alcohol was added to the dye solution to make it neutrally buoyant in fresh water. In both cases the density was matched to better than $2 \times 10^{-3}\%$. However, molecular diffusion led to a gravitational instability of the dye streams after they had been carried some distance from their sources. This instability, despite causing a small amount of lateral spreading, proved useful in that it eventually distributed the dye as a vertical sheet. The most effective positions for these continuous dye sources were found to be within the boundary current. This is because the dye streams are better formed at the larger velocities, at which it was easier to match the tube exit velocity to the ambient velocity, and also because the streams later underwent streamwise convergence as they entered the interior flow, becoming much more visible. Dye release in the interior was successful, but those streams became invisible when stretched on entering the boundary current. Hence most of the outlets were positioned near the west. The dye lines were passively advected along streamlines in the boundary current, passed through the interior of the basin, and eventually re-entered the boundary current. Throughout this circuit the tracer revealed the mean flow, any unsteadiness in the velocity field, eddy shedding, stirring in the interior, and any other small-scale motions. Additional measurements were made of the local velocity profiles by using a solution of bromothymol-blue pH indicator in the water and electrode wires stretched from the centre of the tank to the west wall. The wire was partially insulated so that the line of coloured indicator so formed was broken at 0.5 cm intervals.

The advection of dye or pH indicator was recorded using still and video cameras located above the axis of the tank and a second video camera positioned directly above the northwestern wall. This second camera was framed on the northwest quadrant of the basin and gave a closer view of the boundary current, the separation and the eddy-shedding regions of the flow. Of particular use were time-lapse video records.

Further information on the steadiness or instability of the flow was obtained from self-heated semiconductor thermistor beads. Two of these were mounted at mid-depth in the tank and connected in an electronic circuit which maintained a power supply to the thermistor sufficient to maintain it at a constant temperature despite varying heat fluxes due to varying flow speeds past the bead. The circuit provided an output voltage signal related (in a nonlinear fashion) to the power supplied and hence to the flow speed. In this way the variability of extremely slow flows could be detected. This instrument relied on the water temperature remaining constant throughout the duration of monitoring. Due to the temperature dependence and nonlinearity of the output a calibration against absolute speed was not made and we utilize the voltage output only as an indication of the variability of the flow speed.

3. The numerical model

3.1. *Equations of motion*

The non-dimensional momentum and continuity equations for a homogeneous incompressible fluid relative to a coordinate system rotating with angular velocity Ω are

$$Ro\left[\frac{\partial \boldsymbol{u}}{\partial t}+(\boldsymbol{u}\cdot\nabla)\boldsymbol{u}\right]+2\boldsymbol{k}\times\boldsymbol{u}=-\nabla p+E\nabla^2\boldsymbol{u} \tag{1}$$

and

$$\nabla\cdot\boldsymbol{u}=0, \tag{2}$$

where $\boldsymbol{u}$ is the velocity, p is the pressure and $\boldsymbol{k}$ is a unit vector parallel to Ω. The length, time, velocity and pressure have been scaled by H_0, $|\Delta\Omega|^{-1}$, $|\Delta\Omega|H_0$ and $|\Delta\Omega|\Omega\rho H_0^2$, respectively, where H_0 is the depth at the centre of the basin, $\Delta\Omega$ is the differential angular velocity of the lid and ρ is the fluid density. The importance of advection and viscosity are parameterized by the Rossby number $Ro=|\Delta\Omega/\Omega|$ and Ekman number $E=\nu/\Omega H_0^2$, respectively, where ν is the kinematic viscosity of the fluid. Gravitational and centrifugal accelerations are not relevant to this system, since there is no free surface or stratification. If we define right-handed coordinates fixed to the rotating frame with the origin at the centre of the sloping bottom, the z-axis vertical and the y-axis to the north (see figure 1), no-slip boundary conditions have the form

$$\left.\begin{array}{lll}\boldsymbol{u}=\boldsymbol{0} & \text{on} & r=\dfrac{L}{2H_0}\quad\text{and}\quad z=y\tan\alpha,\\ \boldsymbol{u}=\frac{1}{2}\zeta_T r\hat{\theta} & \text{on} & z=1,\end{array}\right\} \tag{3}$$

where $\zeta_T=2\Delta\Omega/|\Delta\Omega|$ is the relative vorticity of the lid, r is the radial coordinate and $\hat{\theta}$ is the azimuthal unit vector; we have assumed without loss of generality that the lid slope $\tan\alpha_1$ is zero. We shall separate the vertical and horizontal components of the velocity by writing $\boldsymbol{u}=\boldsymbol{u}_H+\boldsymbol{k}w$, where $\boldsymbol{k}\cdot\boldsymbol{u}_H=0$. It is found experimentally that $\boldsymbol{u}_H$ is independent of z outside the Ekman layers on the top and bottom boundaries for the parameters used in this study. Assuming that $\partial\boldsymbol{u}_H/\partial z=\boldsymbol{0}$, the vertical component of the curl of (1) yields the vorticity equation

$$Ro\left[\frac{\partial \zeta}{\partial t}+\nabla_H\cdot(\boldsymbol{u}_H\zeta)\right]-2\frac{\partial w}{\partial z}=E\nabla_H^2\zeta, \tag{4}$$

where $\zeta=\boldsymbol{k}\cdot(\nabla\times\boldsymbol{u})$ is the vertical component of the relative vorticity and ∇_H is the two-dimensional gradient operator. The horizontal component of the vorticity (which would appear in a vortex tilting term) is absent from this equation as a consequence of the assumption that $\partial\boldsymbol{u}_H/\partial z=\boldsymbol{0}$.

Incompressibility and the depth-independence of the horizontal velocity imply that the vortex stretching term $\partial w/\partial z$ is independent of depth, so it can be determined from the conditions for matching the interior vertical velocity to the upper and lower Ekman layers (Pedlosky 1979):

$$w=\tfrac{1}{2}E^{1/2}(\zeta_T-\zeta)\quad\text{at}\quad z=1, \tag{5}$$

$$w=\tfrac{1}{2}E^{1/2}\zeta+\boldsymbol{u}_H\cdot\nabla h\quad\text{at}\quad z=h, \tag{6}$$

where $h=y\tan\alpha$ is the scaled bottom topography, and the weak dependence of the second term in (6) on bottom slope has been neglected (valid for $\tan\alpha=|\nabla h|\ll 1$). The steady, linear Ekman matching conditions used here are valid for flows which are nearly steady over one rotation period (Beardsley 1975) and have $Ro\ll E^{1/4}$ (Bennetts & Hocking 1973). The latter criterion is violated for the more strongly forced results presented here, but the close similarity of the calculated flows to those seen in the laboratory suggests that the error involved in using linear Ekman pumping is insignificant. Using (5) and (6) we find

$$\frac{\partial w}{\partial z}=\frac{E^{1/2}(\frac{1}{2}\zeta_T-\zeta)-\boldsymbol{u}_H\cdot\nabla_H h}{1-h}. \tag{7}$$

Without loss of generality the horizontal velocity can be expressed in terms of a streamfunction ψ and scalar potential ϕ as

$$\boldsymbol{u}_H=\boldsymbol{k}\times\nabla_H\psi+\nabla_H\phi, \tag{8}$$

where

$$\nabla_H^2\psi=\zeta. \tag{9}$$

From (2) we have

$$\nabla_H^2\phi=-\frac{\partial w}{\partial z}, \tag{10}$$

but this is not sufficient to define ϕ due to the presence of ϕ in the orographic term $\boldsymbol{u}_H\cdot\nabla_H h$ in (7). However, since the contribution of the divergent velocity to this term is expected to be small, we can estimate ϕ by neglecting this contribution and treating (10) as a Poisson equation for ϕ. Using this estimate, it was found from numerical experiments that the divergent horizontal velocity $\nabla_H\phi$ is negligible in most of the basin, where the dominance of the topographic Sverdrup or Stommel balances implies that the stretching term is almost zero. (These balances give a non-divergent horizontal velocity, but a divergent horizontal transport $(1-h)\boldsymbol{u}_H$, making a transport streamfunction formulation inappropriate.) The divergent horizontal velocity is largest in the inertial jet, the viscous sublayer of the western boundary current, and the time-dependent region where eddies are shed (under strong forcing), but even in these regions the horizontally divergent velocity was at most only a few percent of the horizontally non-divergent velocity $\boldsymbol{k}\times\nabla_H\psi$. With this in mind, the divergent velocity was neglected in the orographic and advection terms, simplifying the vorticity equation to

$$Ro\left[\frac{\partial\zeta}{\partial t}+J(\psi,\zeta)\right]=2\left[\frac{E^{1/2}(\frac{1}{2}\zeta_T-\zeta)-J(\psi,h)}{1-h}\right]+E\nabla_H^2\zeta, \tag{11}$$

where J is the two-dimensional Jacobian operator. Thus the problem has been reduced to solving (11) and (9), and the no-slip boundary condition becomes

$$\nabla_H\psi=\mathbf{0} \quad \text{at} \quad r=\frac{L}{2H_0}. \tag{12}$$

This formulation is equivalent to the quasi-geostrophic approximation (Pedlosky 1979), except that the finite depth variation has been retained.

3.2. *The numerical scheme*

The numerical experiments were performed using a highly efficient sliced-cylinder code developed by Page (1982) and described in detail in his PhD thesis (Page 1981). The algorithm is essentially the same as that presented by Beardsley (1972), which was in turn based on the refinement by Israeli (1970) of a scheme proposed by Pearson (1965). Briefly, the code is a finite-difference scheme formulated in polar coordinates. Second-order differences were used to represent the spatial derivatives, with flux-conservative operators used for the Jacobian and Laplacian terms – for example, the orographic term was evaluated as

$$\frac{-J(\psi,h)}{1-h}=\nabla_H\cdot[\ln(1-h)\boldsymbol{k}\times\nabla_H\psi]. \tag{13}$$

The terms in the vorticity equation at the central grid point were evaluated using flux integrals through the first circle of grid points around the origin.

The vorticity equation (11) was advanced in time using the alternating-direction implicit method (second-order accurate in time), and a fast Fourier transform in θ was used to solve the Poisson equation (9) for ψ. Since the advection term in (11) couples it nonlinearly to (9) the two equations were solved iteratively within each timestep until ψ and ζ converged. This in-timestep iteration also served to converge ζ at the boundary to a value which was consistent with the no-slip boundary condition (12). The numerical results reported here were obtained using 160 grid points in the radial direction and 512 in the azimuthal direction and a timestep of $0.0125(4\pi E^{1/2})^{-1}$ rotation periods, giving very good spatial and temporal resolution. A uniform grid was used in both directions in order to retain second-order accuracy in the spatial derivatives.

4. Flow structure

4.1. *Laboratory flow regimes*

Photographs of the laboratory flow as revealed by the advection of dye streams under a range of Rossby and Ekman numbers, with anticyclonic forcing, are shown in figure 2. As in previous work with the sliced-cylinder model, the downward pumping by the upper Ekman layer flow drove a broad, slow Sverdrup flow across the lines of constant depth throughout the interior of the basin. The return flow was confined to a fast, narrow boundary current against the western wall and flowing toward shallower water (poleward).

For very small Rossby numbers the circulation possessed close to north-south

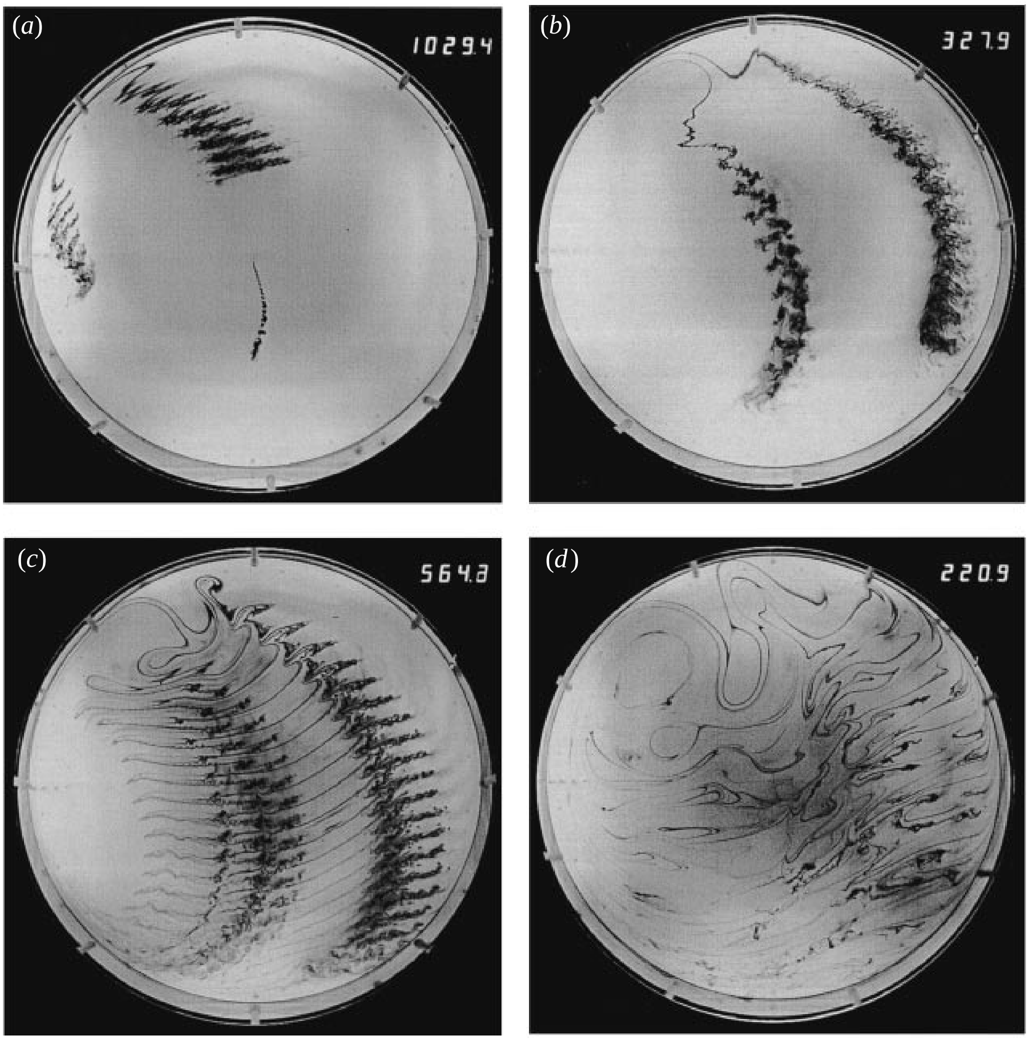

FIGURE 2. Circulation as revealed by dye advection for four sets of conditions which give different flow regimes: (*a*) as close to linear as practicable ($\Omega = 2.000\,\mathrm{rad\,s^{-1}}$, $\Delta\Omega = 0.0225\,\mathrm{rad\,s^{-1}}$, $Ro = 0.0112$, $E = 3.15 \times 10^{-5}$, $Re_\gamma = 46.8$); (*b*) nonlinear but stable ($\Omega = 0.500\,\mathrm{rad\,s^{-1}}$, $\Delta\Omega = 0.0278\,\mathrm{rad\,s^{-1}}$, $Ro = 0.0557$, $E = 1.26 \times 10^{-4}$, $Re_\gamma = 92.1$); (*c*) unstable and periodic ($\Omega = 1.001\,\mathrm{rad\,s^{-1}}$, $\Delta\Omega = 0.0532\,\mathrm{rad\,s^{-1}}$, $Ro = 0.053$, $E = 6.3 \times 10^{-5}$, $Re_\gamma = 139.7$); (*d*) unstable and aperiodic ($\Omega = 0.500\,\mathrm{rad\,s^{-1}}$, $\Delta\Omega = 0.0845\,\mathrm{rad\,s^{-1}}$, $Ro = 0.169$, $E = 1.26 \times 10^{-4}$, $Re_\gamma = 279$). These runs were with a northern-hemisphere orientation (Ω anticlockwise and shallowest water at the top of the image) and had anticyclonic lid forcing. Contours of constant depth are straight lines from left to right. Neutrally buoyant dye was injected near the left wall (at the west) as well as at the centre of the cylinder. The number on each frame shows the time in tank rotation periods (to 0.1 periods) after the beginning of dye release, and the release began long after the flow had adjusted to the applied forcing.

symmetry but was centred far to the west of the basin (figure 2*a*). Streamlines diverged from the boundary current at all latitudes in a manner consistent with linear analysis (Pedlosky & Greenspan 1967; Beardsley 1969). Under these conditions the time required for tracer to be advected around a complete cycle of the basin was many hours, a time so long that convective motions, though extremely small, eventually led to dispersion of the dye streams and poor visualization of the inflow from the interior to the boundary current in the south. When the surface stress was cyclonic the flow was approximately reversed (except that a small oscillation responsible for the kinks in the dye stream in figure 2(*a*) and discussed below was not observed).

The only unexpected feature of the laboratory flow at small Rossby numbers was that the flow was never completely steady under anticyclonic forcing. Even at $Ro \approx 0.002$ a small-amplitude oscillation persisted indefinitely. This oscillation could be detected only where dye streams exited from the boundary current and where the bromothymol-blue indicator lines crossed the edge of the current at the west. It appeared as a small azimuthal fluctuation of the azimuthal velocity and of the dye stream. As a result the dye stream shifted across a narrow band of streamlines and the oscillation was recorded as a regular series of kinks 'fossilised' in the dye line as it was carried through the interior of the basin. These oscillations could not have been introduced by flow past the dye tubes at the west since the Reynolds number based on the tube diameter was too small (between 0.4 and 8) and the same oscillations were found in the thymol blue lines at the outer edge of the current beyond the tubes. Furthermore, the fluctuations were in phase across the whole of the current despite there being two to four dye tubes, each at locations of very different mean velocity. We carried out exhaustive tests to determine whether this small oscillation was produced by unwanted forcing from imperfections in the operation of the rotating lid apparatus. Hence the lid was changed, the supporting mechanism was modified and reconstructed, and a micrometer needle gauge was used to make *in situ* measurements of fluctuations in the position of the bottom surface of the lid. The changes produced no effects on the observed oscillations. The measurements also indicated that the vertical displacements of the driving surface were less than 5% of the Ekman layer thickness and that the vertical velocities of the surface were three orders of magnitude smaller than the vertical Ekman pumping velocity. From this we expect any imperfections to have negligible and undetectable effects on the flow. On the other hand, we note that even the smallest Rossby number achieved does not satisfy the criterion for linear flow ($Ro \ll E^{1/2}$; Becker & Page 1990) since $0.006 < E^{1/2} < 0.014$ and so the theory does not predict steady flow. The oscillations were modulated in such a way that there was an integer number in each revolution of the lid (see § 5.5), indicating that the flow may have been extremely sensitive to weak forcing at frequencies near the lid rotation frequency. Nevertheless, the measured frequencies will provide evidence that whatever process led to the oscillations in the stable regime, it is unrelated to the shear flow instability mechanism at work under stronger forcing as reported below.

With stronger forcing the flow became increasingly asymmetric in the north-south direction and the western boundary current intensified to the north (figure 2*b*) in the manner observed in previous studies. The outflow from the boundary current became less divergent, until it became a narrow jet. As an illustration of this, the photograph in figure 2(*b*) shows two streamlines initially 2 cm apart at the west (with the outer dye tube 1 cm from the wall). The lines did not diverge significantly until the jet had penetrated some distance southeastward into the interior. At this point the jet underwent a rapid divergence, a part of it looping northward and supplying the return flux to the eastern portion of the basin and a part of it turning westward to supply the western portion of the interior. This westward portion of the flow enveloped a region of closed anticyclonic recirculation (made visible in other runs by placing dye tubes slightly farther than 3 cm from the wall at the west). A second region of closed recirculation persisted farther south near the west. Also visible was a narrow eastern boundary layer approximately 0.5–1 cm wide along the full length of the eastern wall which carried a relatively small flux of water northward and upward along the wall to the lid. A similar upward flow (again of order 0.5–1 cm thick) was seen on the western wall inside the boundary current, again feeding water into the radial Ekman flux at the lid. This boundary layer upflow placed a lower limit on the distance from the wall at which tracer, released at the west, marked streamlines that entered the interior before entering the upper Ekman layer. A bottom Ekman layer which carried a weak flux to the east was observed in the interior on occasions when some of the dye fell to the bottom after double-diffusive finger instability.

For still larger forcing the amplitude of the flow oscillations became so large that they led to eddy shedding in the region where the separated boundary current jet entered the interior flow (figure 2*c*). This instability was associated with rapid adjustment of the flow from the narrow free jet to the broad, slow interior flow that filled the rest of the basin. At marginally supercritical conditions the oscillations and attendant eddy shedding were precisely periodic. The most obvious eddies were cyclones which, after generation from the 'flapping' jet, moved westward around the edge of the anticyclonic recirculating gyre. The relative vorticity of each cyclonic eddy was largely dissipated by the time the eddy had approached the outer edge of the western boundary current, from where the tracer carried by the eddy was passively advected southward with the interior flow. Only a small outer part of each eddy was entrained into the anticyclonic gyre. At Rossby numbers larger than that required for generation of cyclones, anticyclonic eddies formed in the northeast of the basin, where the eastward portion of the diverging boundary current jet turned southward again to enter the slow interior drift. These too were spun-up before they were advected far. One result of the instability was a very extensive stirring of tracer from any streamline in the jet across much of the width of the basin. The distribution of passive tracer in the interior in experiments such as that in figure 2(*c*) is a 'fossilised' record of this stirring. Superimposed on the mean flow and on the fossil tracer pattern in all unstable runs were westward-travelling wave-like oscillations throughout the basin. These had amplitudes which increased with *Ro* and are assumed to be Rossby waves excited by the jet oscillation and eddy shedding.

In some experiments in which the flow was periodic, we identified a second frequency within the flow, corresponding to an alternation between larger and smaller eddies. There is some evidence that the second frequency tended to occur only for forcing strengths well beyond that required for instability.

When still greater forcing was applied, as in figure 2(*d*), the periodic flow gave way to a regime in which the flow never precisely repeated. Intervals between consecutive eddies were measured over sequences of 20 to 40 eddies from the video records and found to vary significantly. There were also no regular patterns in the distribution of passive tracer produced in the interior by the eddy-shedding process. The output from the thermistor speed probes, which provided much longer and continuous records more suited to analysis of the temporal behaviour at fixed points in the flow, confirmed the aperiodic nature of the flow and will be discussed in § 5. In this aperiodic regime the flow was more energetic, the intense anticyclonic gyre in the northwest was larger and Rossby waves in the interior had larger amplitudes. The cyclonic eddies now took a range of sizes. Some were swept around in the anticyclonic gyre, some were advected southward as at lower Rossby numbers, and others were torn apart by the mean flow where it divided between the recirculating gyre and the southward interior flow. Strong anticyclonic eddies were the dominant feature to the northeast of the separated boundary current.

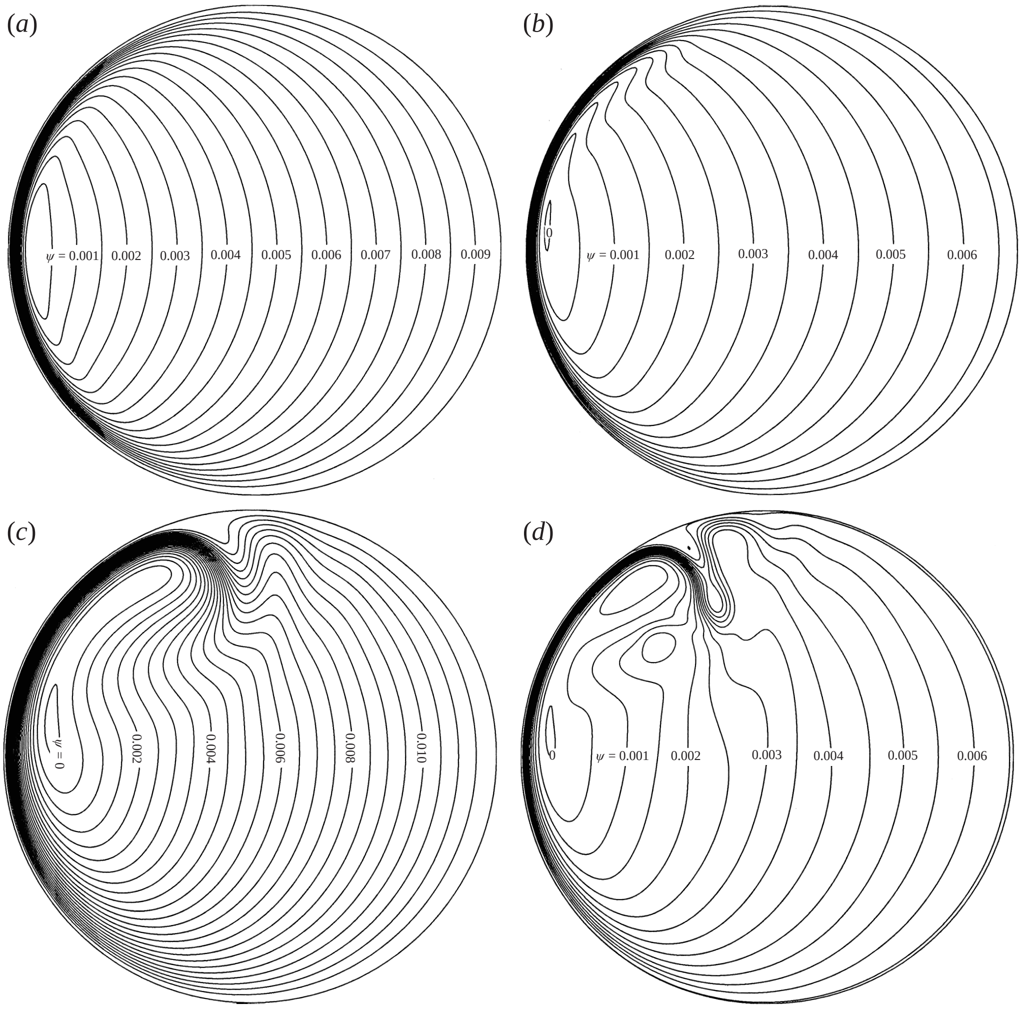

FIGURE 3. Streamlines from the numerical model with $\tan\alpha = 0.1$ and $L/H_0 = 7.84$: (*a*) linear flow: $Ro = 0$, $E = 6.27 \times 10^{-5}$; (*b*) quasi-linear regime: $Ro = 0.01$, $E = 3.14 \times 10^{-5}$; (*c*) nonlinear regime: $Ro = 0.06$, $E = 1.25 \times 10^{-4}$; (*d*) periodic eddy-shedding regime: $Ro = 0.0393$, $E = 3.14 \times 10^{-5}$. The streamfunction is defined as in § 4.4 (scaled by $Ro\Omega L^2$, with $\psi = 0$ on the point of maximum western boundary current transport through $y = 0$) to allow comparison with figure 9, but note that the bottom slopes are different.

4.2. *Quasi-geostrophic model results*

Around 130 numerical experiments were conducted in order to explore the flow behaviour for a variety of different basin widths and Rossby and Ekman numbers. As in the laboratory experiments, the flow behaviour passed through a number of regimes for increasing values of *Ro*. For very weak forcing, the circulation pattern had a near north-south symmetry and the flow was steady (streamfunction contours are shown in figure 3*a*). The western boundary current intensified to the north under stronger forcing (figure 3*b*), and a further increase in forcing resulted in separation of the boundary current, which penetrated into the interior as a jet (figure 3*c*). Even stronger forcing yielded a transition to periodic unstable flow, with cyclonic eddy shedding

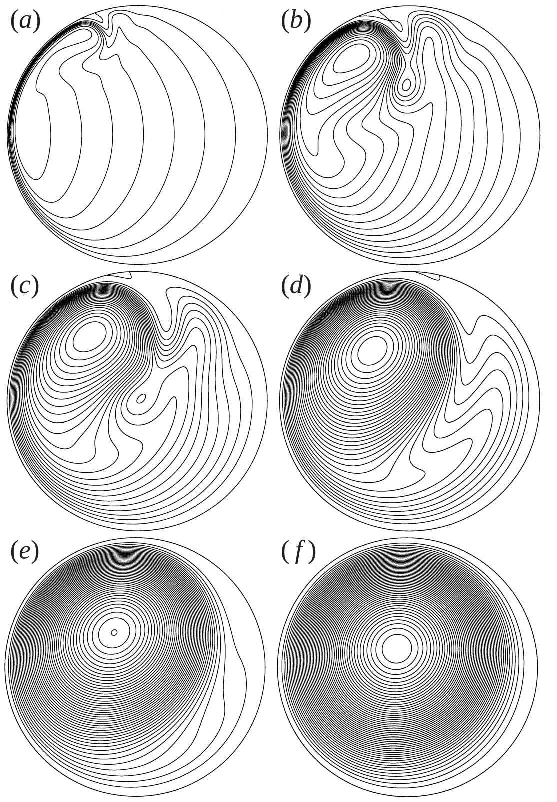

FIGURE 4. Streamlines from the numerical model for various L, with fixed $H_0 = 12.5\,\mathrm{cm}$, $\tan\alpha = 0.1$, $E = 3.14 \times 10^{-5}$ and $Ro(L/H_0) = 0.218$ (so $Re_\gamma = Ro\, E^{-2/3}(L/H_0)(\tan\alpha)^{1/3} = 102$). (*a*) $L/H_0 = 7.84$ (as in the laboratory experiments reported here); (*b*) $L/H_0 = 3.92$; (*c*) $L/H_0 = 2.77$; (*d*) $L/H_0 = 1.96$ (similar to Beardsley 1969, 1973 and Beardsley & Robbins 1975); (*e*) $L/H_0 = 1.39$; (*f*) $L/H_0 = 0.980$) (similar to Becker & Page 1990). The streamfunction is scaled by $Ro\Omega L^2$, with $\psi = 0$ on the boundary and the same contour interval for all plots.

from the cyclonic loop in the boundary current jet (figure 3*d*); shedding of anticyclonic eddies at larger *Ro* was less prevalent than in the laboratory results. Further transitions to alternating eddy sizes (period doubling) and to aperiodic eddy shedding took place when the forcing was very strong. However, under these conditions the advective term in the vorticity equation was not accurately represented by second-order finite differences in the strongly decelerating flow in the separated jet, due to the numerical instability discussed by Leonard (1984). This numerical limitation and the questionable validity of the quasi-geostrophic formulation with linear Ekman layers for strongly nonlinear flows prevented us from using the numerical model to accurately investigate the aperiodic regime. Another limitation of the quasi-geostrophic formulation was its inability to include the upward Ekman return flux seen close to the sidewalls in the laboratory, so the eastern boundary layer was absent from the numerical results.

The effects of changing the basin width were also studied using the numerical model. Figure 4 shows streamfunction plots of the solution for the same values of $Ro(L/H_0)$, E and $\tan\alpha$ in basins of the same depth (and thus the same values of $Re_\gamma = RoE^{-2/3}(L/H_0)(\tan\alpha)^{1/3}$ and $\beta = 2\Omega\tan\alpha/H_0$) but different width. (Note that the contrasts would be further accentuated if we had chosen to compare solutions for a fixed *Ro*.) It can be seen that in the wide basin used in our experiments the boundary current separation and eddy shedding are much less influenced by the eastern boundary than is the case for aspect ratios of order one. In narrow basins the flow is dramatically stabilized, to the extent that the western boundary current continues past the most poleward point and separates in the east, as was reported by Becker & Page (1990) for the case of cyclonic forcing. Hence wide basins are of most interest for studies of nonlinear phenomena.

Further results from the numerical model for the interior and boundary current velocities and for the boundary current width are discussed below alongside the corresponding laboratory measurements. A comparison with quantitative information on the streamlines for the laboratory flow (§ 4.4) is given after we have presented the velocity measurements, and results for the location of boundary current separation (§ 6) are delayed until after the conditions for instability are determined (§ 5).

4.3. *Flow velocities*

The results of our measurements and computations of flow velocities are reported only briefly, since they are not dissimilar to those of Beardsley (1969, 1973) and Beardsley & Robbins (1975). Examples of velocity profiles across the laboratory boundary currents and those given by the numerical model, normalized by the velocity $a\Omega Ro$ and radius $a = L/2$, are plotted in figures 5(*a*) and 5(*b*), respectively. The agreement is excellent. The only difference is a slightly smaller maximum current speed in the experiment shown, and several experiments show that this is not a consistent difference but associated with scatter in the data. No significant depth dependence was detected in the experiments. Some of the small differences between the four measured profiles shown are a result of small-amplitude oscillations in the flow, particularly at the edge of the boundary current. The interior southward drift was found to be independent of x to the precision of the measurements (10%) and constant to within 20%. The profiles provide values of the maximum northward current speed v_{max} and the current widths δ_m and δ_0 defined by the positions of the maximum speed and velocity reversal, respectively.

The normalized maximum northward velocities along $y = 0$ are plotted in figure 6(*a*) for a number of experiments in the low-Rossby-number regime, along with the results of the numerical model. In order to remain within the quasi-linear regime (defined as the conditions under which there was little downstream intensification of the boundary current) in the experiments it was not possible to cover a range of E at a fixed value of Ro. Hence the experiments covered a range of both Rossby and Ekman numbers and in this regime it was difficult to determine independently the role of each parameter. The quasi-geostrophic model, on the other hand, reveals a dependence on both Ro and E, and the laboratory data are fully consistent with these. Figure 6(*b*) shows a transition at finite Rossby number from v_{max} independent of Rossby number at $Ro \ll E^{1/2}$ to $v_{max} \sim Ro^{-0.6}$ at $Ro > 0.05$ (for $E = 6.27 \times 10^{-5}$). We also find, for example, $v_{max}/a\Omega Ro \sim E^{0.13}$ for $Ro = 0.02$ (figure 6*a*).

The distance δ_m from the wall to the position of maximum velocity lay in the range 1.5 to 2.0 cm (or $0.013 < \delta_m/L < 0.02$) in all of the experimental runs in the quasi-linear regime. However, this position could not be measured with sufficient precision to reliably show its dependence on the external parameters. Measurements of the full width δ_0 of the current lay in the range $0.04 < \delta_0/L < 0.10$ and showed that it increased with both Rossby and Ekman numbers, consistent with the predictions of the quasi-geostrophic model. The latter gives $\delta_m/L = 0.255E^{0.325}$ for $Ro = 0.01$ ($\delta_m \sim E^{1/3}$ is expected from linear theory). For the full width it gives, for example, $\delta_0/L = 1.53E^{0.328}$ (on $y = 0$) for $Ro = 0.02$, and for $E = 6.27 \times 10^{-5}$ the width on

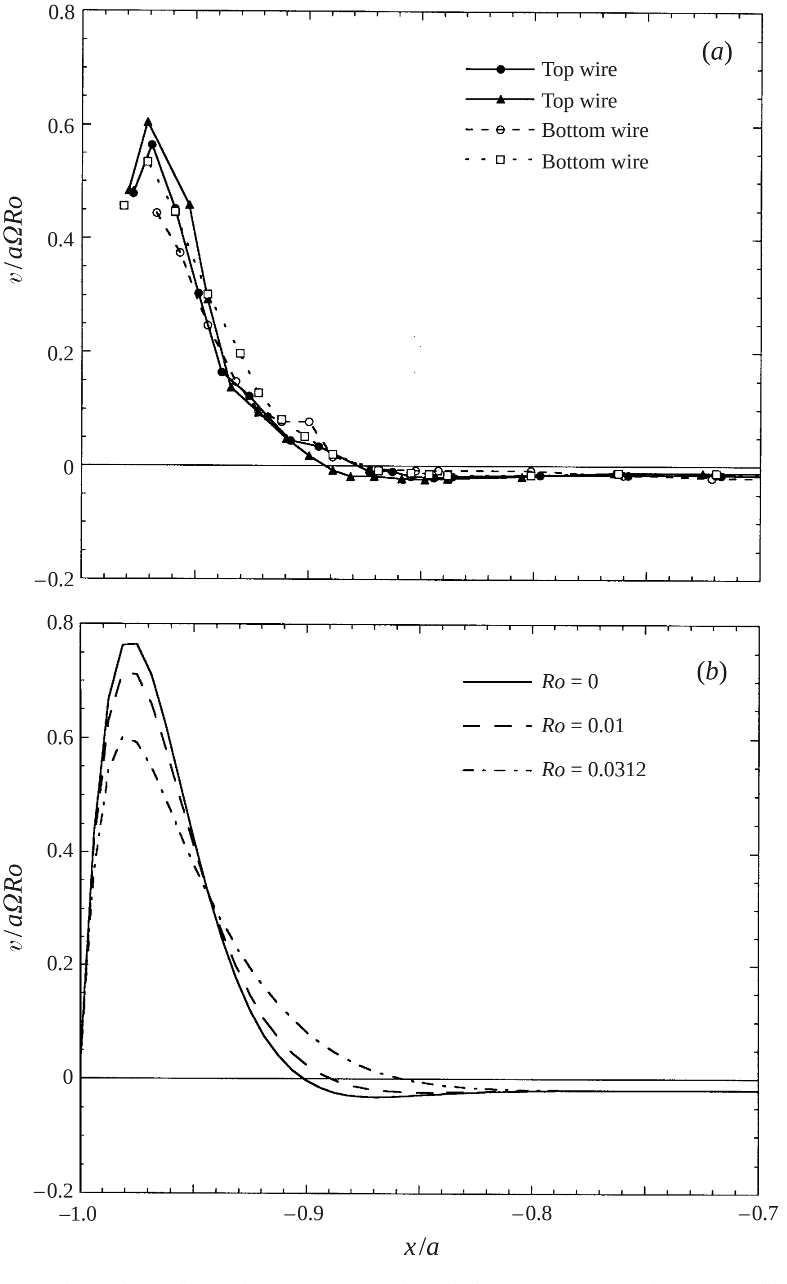

FIGURE 5. Examples of profiles of the northward velocity component along a radial line from the west wall to the centre of the cylinder, obtained (*a*) from the bromothymol-blue technique with electrode wires 2 cm below the lid and 2 cm above the base ($\Omega = 1.00\,\text{rad}\,\text{s}^{-1}$, $Ro = 0.010$, $E = 6.3 \times 10^{-5}$, anticyclonic forcing) and (*b*) from the quasi-geostrophic model for three values of Ro and $E = 6.27 \times 10^{-5}$.

$y = 0$ increases from 0.049 at $Ro < E^{1/2}$ to ~ 0.1 at $Ro \sim 0.1$, largely as a result of the centre of the gyre moving more northwards for large Ro.

The north-south component v_{int} of the interior velocity (figure 7) was measured using both the bromothymol-blue technique and the advection of the dye streams (as

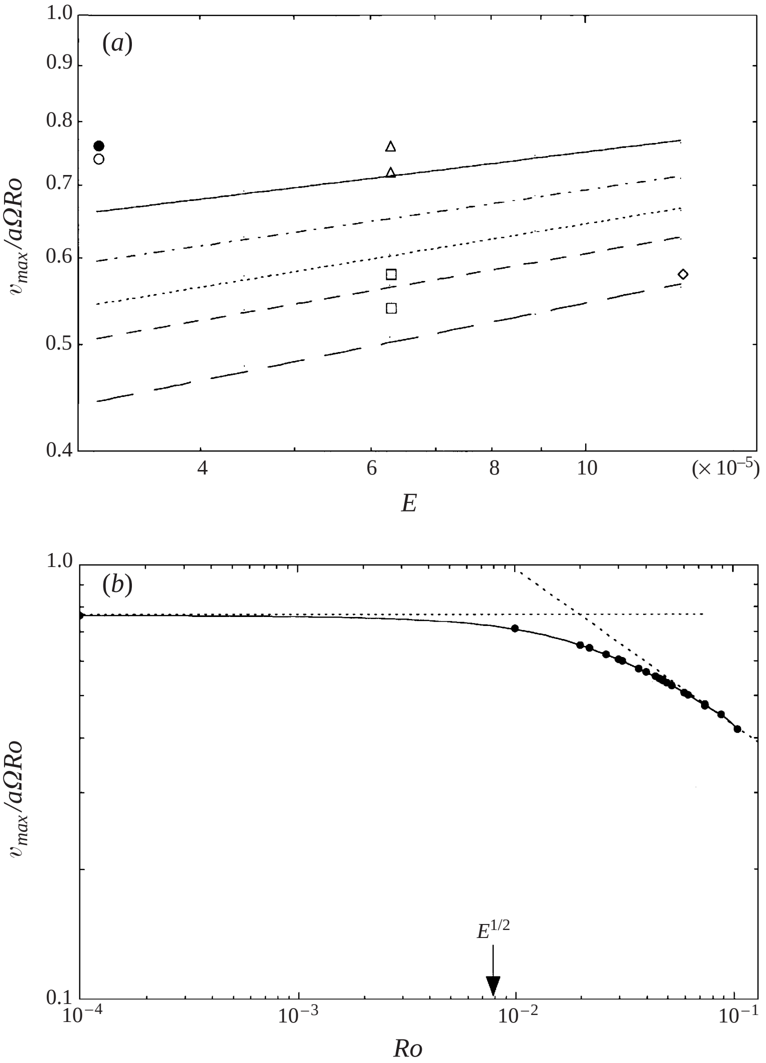

FIGURE 6. (*a*) The normalized maximum northward velocity measured in the western boundary current at the west for experiments having $\tan\alpha = 0.10$ and a range of Rossby number (●, $Ro = 0.0026$; ○, $Ro = 0.0051$; △, $Ro = 0.0102$; □, $Ro = 0.0209$; ◇, $Ro = 0.0426$) in the quasi-linear regime, plotted against Ekman number. This lines are from the quasi-geostrophic model: ———, $Ro = 0.01$; — · — · —, $Ro = 0.02$; ....., $Ro = 0.03$; - - - - -, $Ro = 0.04$; —— ——, $Ro = 0.06$. (*b*) The numerical model prediction of maximum northward current velocity on $y = 0$ as a function of Ro for $E = 6.27 \times 10^{-5}$.

seen in figure 2) over a range of Rossby and Ekman numbers and for two values of the slope $\tan\alpha$. No dependence of v_{int}/Ro on Ro could be detected and the velocity varied in a manner consistent with $v_{int} \sim E^{1/2}/\tan\alpha$, as predicted for a Sverdrup balance (Beardsley 1969). Our data give

$$v_{int}/a\Omega Ro = -0.24(\pm 0.02)E^{1/2}/\tan\alpha. \tag{14}$$

For two runs the velocity profile at the west was integrated to find the northward volume flux in the boundary current. The result matched the southward flux in the interior across the vertical plane $y = 0$ $(\delta_0 - L/2 < x < L/2)$ to within 10%. For

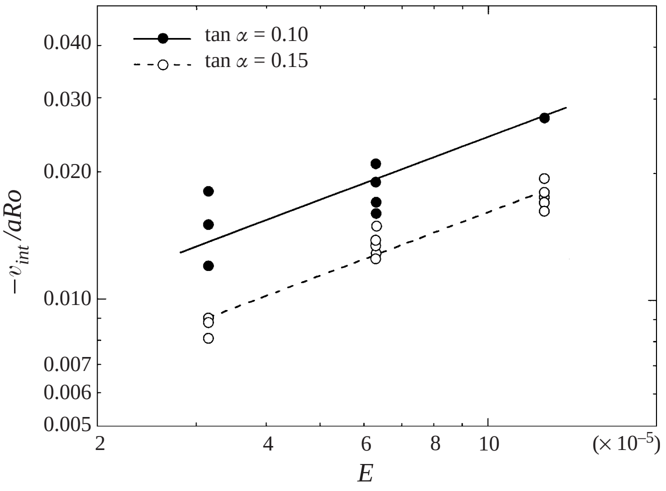

FIGURE 7. Normalized northward velocity component in the interior of the basin (at $y = 0$) for two depth gradients and a range of Rossby numbers, plotted against the Ekman number. The velocity showed no significant variation for $-0.5 < x/a < 0.5$ across the east-west diameter of the basin, and the data represent averaged measurements across this section. The power law of best fit has exponent $\frac{1}{2}$.

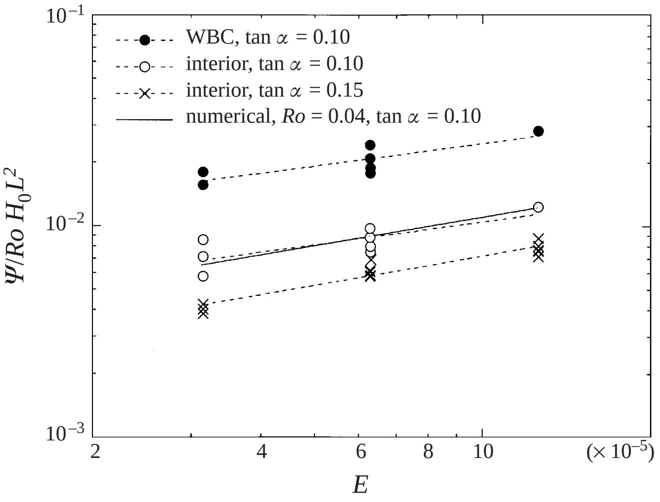

FIGURE 8. Northward volume fluxes across $y = 0$ in the interior of the laboratory model, along with a measure of the boundary current flux (not to be compared in absolute value). The normalized western boundary current transport given by the numerical model for $Ro = 0.04$ and $\tan\alpha = 0.1$ is also shown. The lines have exponent 0.41 ± 0.05.

a larger number of runs we simply calculated the flux $\Psi_B = v_{max}\delta_0 H_0$ (with no adjustment for the shape of the velocity profile) and, in figure 8, compare this with the total southward transport Ψ_{int} in the interior calculated from $\Psi_{int} = -v_{int}H_0L(1 - \delta_0/L)$. A small northward flux in the viscous eastern boundary current was neglected. The interior transport, normalized by $Ro\Omega L^2 H_0$, for $\tan\alpha = 0.10$ is described by the regression

$$\Psi_{int}/Ro\Omega L^2 H_0 = 0.030E^{0.36}/\tan\alpha, \qquad (15)$$

and the same power law is obtained as the best fit to the boundary current flux. The data for $\tan\alpha = 0.15$ are better described by the power law $\Psi_{int}/Ro\Omega L^2 H_0 \sim 0.079E^{0.46}/\tan\alpha$ but are not inconsistent with (15), where the constant is again 0.030.

On figure 8 we also plot the western boundary current transport derived from the quasi-geostrophic model for $Ro = 0.04$. We find only a small dependence of the normalized transport on Ro, and a transport increasing as $E^{0.454\pm0.004}$ for Ro in the range 0.01 to 0.06. The quasi-geostrophic model is therefore consistent with the measurements, the absolute values lying within 10% of each other across the range of E. Note that whereas the interior velocities are in accord with linear theory, the finite width of the boundary current contributes to a reduction in total interior (and hence boundary current) transport.

4.4. *Experimental streamfunction*

From the velocity measurements it was possible to determine streamfunction contours for the laboratory flows. First, from the video records we constructed the pattern of streamlines throughout those regions of the circulation which were steady apart from small-amplitude Rossby wave oscillations. This required tracking of passive tracer in the interior flow over times very much longer than the wave period. It was not attempted for the aperiodic regime, in which oscillations were of larger amplitude and where dye did not form regular patterns in the interior. By combining the streamline information with the estimates for total transport we determined those streamlines which represented equal intervals in the velocity streamfunction $\psi = \int_{x_0}^{x} v\,\mathrm{d}x$, where x_0 is the location of the outer edge of the boundary current (note that this is a different definition for ψ from that in § 3.1). This task was simplified by the observation that the southward velocity component v across $y = 0$ in the interior was to a good approximation independent of the east-west position x (outside the narrow boundary layer on the eastern wall).

Examples of the resulting streamfunction contours for experiments in each of the flow regimes (other than the aperiodic regime) are shown in figure 9, where ψ is scaled by $Ro\Omega L^2$. The streamlines sketched within the unsteady eddy-shedding region for the unstable case are not well-defined and are intended to only approximately indicate the mean flow. The major features of the circulation have already been noted in reference to figure 2, and the results can be compared with the computed streamfunctions in figure 3, noting that the difference in total transport is due to a different bottom slope. One feature that is clear in the experiments but cannot appear in the quasi-geostrophic model is the tendency for streamlines to approach the eastern boundary. This is another indication of a small but significant transport from the interior into the viscous eastern boundary current and thence to the upper Ekman layer. Otherwise, the quasi-geostrophic model and the measurements give very similar results, even at relatively large Ro.

5. Stability boundaries

5.1. *Critical external parameters*

The onset of instability and the transition between periodic and aperiodic flow were located in parameter space using the flow visualization. Each run was classified as quasi-linear, nonlinear but stable (having the boundary current outflow localized to a jet in the northwest, but no eddy-shedding), unstable and periodic, or unstable and aperiodic (figure 10). We have defined instability here as the formation and shedding of *cyclonic* eddies, since these always formed under forcing weaker than that required

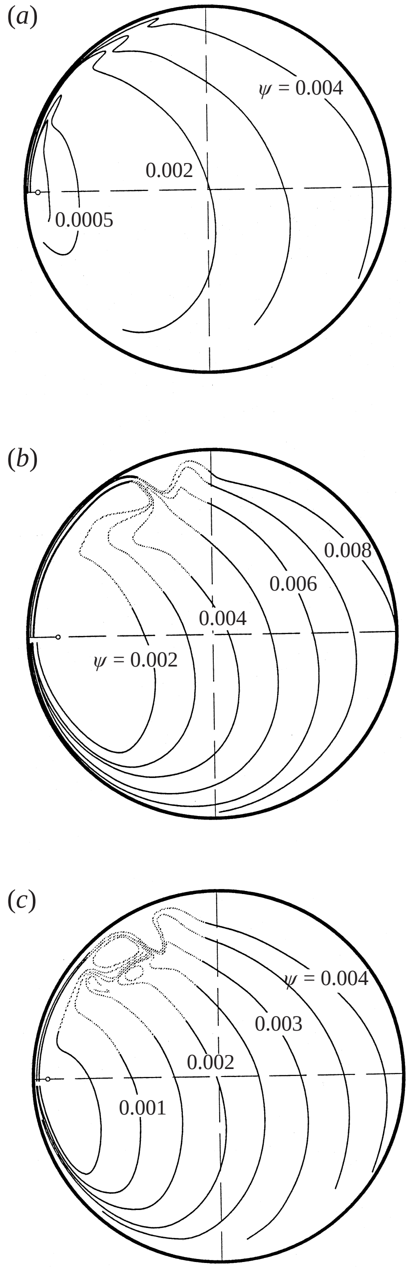

FIGURE 9. Examples of streamlines obtained from laboratory experiments in three flow regimes. The (mean) streamlines throughout the basin are averaged over only small-amplitude wave motions and their positions in the interior are accurate to within ± 0.6 cm ($\pm 0.006L$), whereas those in the highly unsteady eddy-shedding region could not be determined rigorously and are only an approximate indication of the mean flow there. The streamlines shown are at round values of the normalized streamfunction and were obtained by interpolation of a much larger set determined from the video record of dye advection. $\tan\alpha = 0.15$, $L/H_0 = 7.84$. (*a*) Quasi-linear regime, $Ro = 0.011$, $E = 3.15 \times 10^{-5}$, $Re_\gamma = 46.8$; (*b*) nonlinear stable $Ro = 0.067$, $E = 1.26 \times 10^{-4}$, $Re_\gamma = 110$; (*c*) unstable periodic $Ro = 0.039$, $E = 3.15 \times 10^{-5}$, $Re_\gamma = 162$ (defined in § 5.2). Note that the Rossby and Ekman numbers used are close to those in figures 3(*b*), 3(*c*) and 3(*d*), but the bottom slope is different.

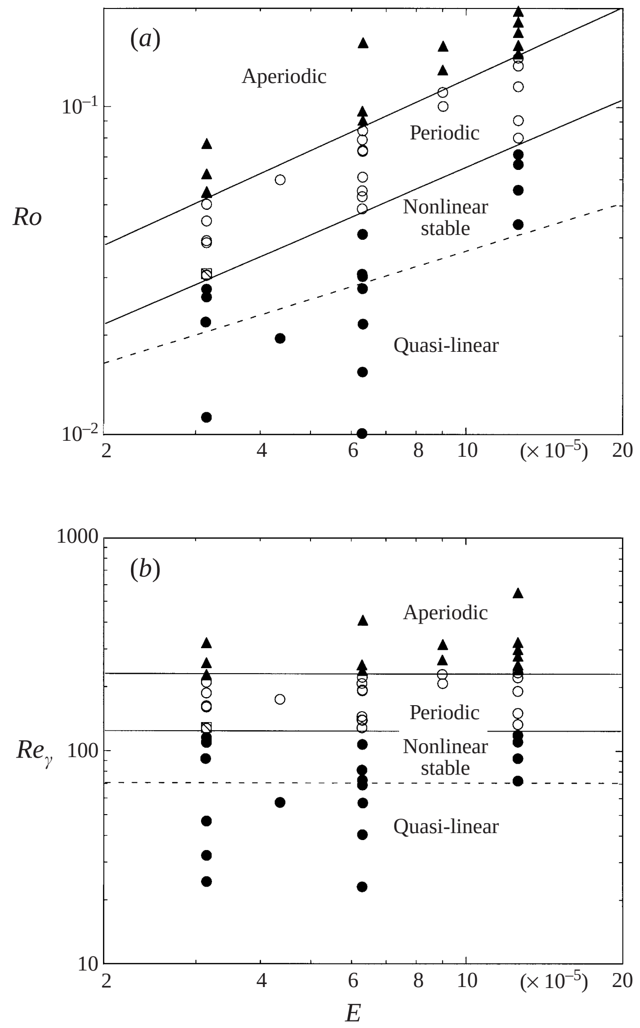

FIGURE 10. Laboratory flow regimes identified with anticyclonic forcing. Transitions from stable (●) to unstable flow with periodic eddy shedding (○) and thence to aperiodic eddy shedding (▲) occur at conditions given by (16) and (17), respectively. The dashed line separates all experimental runs classed as 'quasi-linear' from those classed as 'nonlinear'. Behaviour is shown as a function of: (*a*) external Rossby and Ekman numbers; (*b*) internal Reynolds number and the Ekman number.

to produce anticyclonic eddies. The onset of closed anticyclonic eddies in the northeast was not so readily apparent.

The onset of instability and the transition to aperiodic flow are both well described by simple power-law relations between *Ro* and *E* (figure 10*a*). Onset of eddy-shedding occurred at

$$Ro_1 = (33 \pm 4)E^{0.68 \pm 0.03} \tag{16}$$

and chaotic behaviour was found above the curve

$$Ro_2 = (93 \pm 3)E^{0.71 \pm 0.03}. \tag{17}$$

The transition from quasi-linear to nonlinear flow was less well-defined. At the largest Ekman number (smallest Ω), even the smallest Rossby number achieved gave significant nonlinearity in the flow. However, the data are sufficient to conclude that the effects of nonlinearity were large at Rossby numbers above the broken line on figure 10(a):

$$Ro_0 = 3.6E^{0.5\pm 0.1}. \tag{18}$$

These laboratory results will be discussed further before making a comparison with the numerical model.

5.2. *Instability mechanism*

The onset of instability in either a sliced cylinder (Beardsley 1969; Beardsley & Robbins 1975) or a barotropic rectangular basin (Bryan 1963; Kamenkovitch *et al.* 1995) has previously been located in terms of a Reynolds number for the flow, and the instability in these models has been attributed both to shear instability (Beardsley 1969; Becker & Page 1990) and to the breaking of a large-amplitude standing Rossby wave (Beardsley & Robbins 1975). However, the critical value of the Reynolds number used previously for sliced-cylinder experiments was a function of the Ekman number. The values were also much larger than the critical values of the same parameter evaluated in the present experiments. We therefore explore the flow regimes in terms of several different Reynolds numbers.

An external Reynolds number Re_L can be defined based on the imposed scale $U = \Delta\Omega L/2$ for the maximum velocity and the full width L of the basin, in which case

$$Re_L = UL/\nu = \tfrac{1}{2}RoE^{-1}(L/H_0)^2. \tag{19}$$

For this parameter the relations (16)–(18) indicate that each of the transitions occurs at smaller values of Re_L for larger Ekman numbers (e.g. $Re_{L1} \sim E^{-0.32}$). Hence there seems little value in using such a Reynolds number.

Alternatively, we can consider the Reynolds number based on scales for the maximum velocity (U) and the width ($\delta_i \sim (v_S/\beta)^{1/2}$) of an inertial western boundary current, where $\beta = f\tan\alpha/H_0$ and $v_S = \tau/\beta L H_0 = (\nu/\Omega)^{1/2}\Delta\Omega/\tan\alpha$ is the Sverdrup velocity. This parameter becomes

$$Re_{WBC} = U\delta_i/\nu = \tfrac{1}{4}Ro^{3/2}E^{-3/4}(L/H_0\tan\alpha). \tag{20}$$

Equivalently, we can derive from this the simpler combination $RoE^{-1/2}(L/H_0\tan\alpha)^{2/3}$ which might be utilized as a Reynolds number. The same combination of Ro and E (but with different functional dependence on aspect ratio and bottom slope) is obtained if a Reynolds number is formed using either the interior Sverdrup velocity v_S with the basin width L, giving

$$Re_{Sv} = v_S L/\nu = RoE^{-1/2}(L/H_0\tan\alpha), \tag{21}$$

or the vertical Ekman pumping velocity, $w_E = (\nu/\Omega)^{1/2}\Delta\Omega$, with the water depth H_0, giving

$$Re_E = w_E H_0/\nu = RoE^{-1/2}. \tag{22}$$

The latter parameter, Re_E, is the Reynolds number employed in Beardsley's sliced-cylinder studies to describe the observed onset of the eddy-shedding instability. In those experiments instability occurred at $Re_{E1} \approx (11.3 \pm 0.2) + (1.26 \pm 0.05) \times 10^5 E$. Expressing the new results in figure 10(a) and (16) in a similar linear relation (for more ready comparison) we find the smaller values $Re_{E1} \approx 4.67 + 1.67 \times 10^4 E$. (Alternatively, we prefer to use power laws to relate flows which we expect to be dynamically similar and we find, from (22) and (16)–(18): $Re_{E0} \approx 3.6$, $Re_{E1} \sim E^{0.18}$ and $Re_{E2} \sim E^{0.20}$, where number subscripts again identify the transitions (16)–(18). Thus we have two problems: a critical value of the Reynolds number that is dependent on conditions in a given apparatus, and a disparity in the critical value between two laboratory tanks. The smaller values of Re_{E1} in our experiments are consistent with a dependence of the critical value of Re_{E1} on aspect ratio. This aspect-ratio dependence would be removed if the alternative parameter Re_{Sv} were used. However, use of Re_{Sv} introduces a dependence of each transition on $(\tan\alpha)^{-1}$ and does not remove the Ekman-number dependence. Thus there appears to be no benefit in using the above internal Reynolds numbers in place of the external Reynolds number (19) or the Rossby number.

An alternative Reynolds number, utilized by Kamenkovitch *et al.* (1995). Sheremet *et al.* (1995) and Meacham & Berloff (1997) in their recent numerical studies of the dependence of wind-driven flow on forcing strength, carries similar problems. Kamenkovitch's Reynolds number is based on the *interior* Sverdrup velocity v_S and the inertial *boundary current* width δ_i and can be written as

$$Re_S = v_S\delta_i/\nu = 2^{-1/2}Ro^{3/2}E^{-1/4}(\tan\alpha)^{-2}. \tag{23}$$

This Reynolds number is equivalent to the ratio of inertial and viscous boundary layer width scales $(\delta_i/\gamma)^3$, where $\gamma = (\nu/\beta)^{1/3}$ is the width scale for a purely viscous boundary layer in the linear regime. Kamenkovitch *et al.* (1995) carried out runs with a single Ekman number and obtained one critical Re_S for onset of instability and another (higher) value for transition to aperiodic flow. Other values of E were not explored. We note that a fixed critical value of this parameter would give transitions at $Ro \sim E^{1/6}$, whereas both our data and that of Beardsley (1969) for the sliced cylinder show that the onset of instability and the transition to aperiodic flow occur at values of $Re_S \sim E^{3/4}$ (where we have used relations (16) and (17)). This Reynolds number also does not include a dependence of the onset of instability on the basin aspect ratio, in contrast with the empirical evidence. More fundamentally, a Reynolds number based on the *interior* Sverdrup velocity and a boundary current width does not have a clear physical interpretation in terms of the relative roles of inertial and viscous forces in the boundary current jet.

A Reynolds number that may tell us more about the dynamics of the flow is that based on the boundary current velocity scale v_{max} and the width γ of a viscous boundary layer. The viscous layer width defined above from linear theory can be expressed as $\gamma = (\nu/\beta)^{1/3} = H_0[E/(2\tan\alpha)]^{1/3}$ (Beardsley 1969) and both our experiments and numerical model (§4.3) show very similar dependence of boundary current widths on Ekman number. Linear theory predicts that the interior Sverdrup velocity $v_{int} \sim E^{1/2}$, so that in a very wide basin the total transport $\psi_{int} \sim E^{1/2}$ and the boundary current velocity varies as $E^{1/2}/\gamma \sim E^{1/6}$. On this basis Ierley & Young (1991) used the Reynolds number ψ/ν. On the other hand, our measurements and numerical model results (for all nonlinear flows) show that the dependence of v_{max} on E is a function of Rossby number and that the dependence under conditions anywhere near the observed flow transitions is much weaker (figure 6*a*) than that given by the linear theory. For example, $v_{max} \sim E^{0.13}$ at $Ro = 0.02$. Thus we modify Ierley & Young's Reynolds number by using the velocity scale U independent of viscosity, and write the Reynolds number (after omitting for simplicity a multiplier of $2^{-2/3}$):

$$Re_\gamma = U\gamma/\nu = Ro\,E^{-2/3}(L/H_0)(\tan\alpha)^{1/3}. \tag{24}$$

From (16), (17), to within the experimental uncertainties, the observed transitions in our experiments occurred at $Ro \sim E^{2/3}$. They therefore occurred at a fixed value of Re_γ, a result which is clear when the data are replotted in terms of this parameter (figure 10*b*). At onset of instability we find $Re_{\gamma 1} = 123 \pm 4$ and at transition to chaotic flow $Re_{\gamma 2} = 231 \pm 5$. In addition, the flow became very nonlinear for Reynolds numbers $Re_\gamma > 70 \pm 10$.

To explore further the role of Re_γ we note that the Rossby number at onset of instability (for a given E) is 2.9 times smaller in our apparatus than in the smaller cylinder of Beardsley (1969), a difference almost equivalent to an inverse proportionality to the aspect ratio L/H_0 ($L/H_0 = 7.84$ in our case and 1.99 in the earlier work). Earlier experiments by Pedlosky & Greenspan (1967) used an even smaller aspect ratio ($L/H_0 = 1.42$) and onset of instability in that case occurred at still larger values of Ro. When the larger depth gradient in many of Beardsley's runs ($\tan\alpha = 0.176$) is taken into account, the weak dependence of Re_γ on $\tan\alpha$ brings the critical values of Re_γ further into line with that from the present experiments. From the linear relationship for the critical value of $Re_E(E)$ at onset of instability given by Beardsley we have evaluated $Re_{\gamma 1} = 96 \pm 3$ for his experiments at $E < 3 \times 10^{-5}$, increasing to 107 ± 3 at $E = 6 \times 10^{-5}$. Thus there was only a 10% variation of the critical value of Re_γ across the range of conditions used, and the values are 25% smaller than in the present experiments. Beardsley's values are also slightly smaller than the value $Re_{\gamma 1} = 111 \pm 10$ found from the numerical model with $L/H_0 = 1.96$, $E = 3.14 \times 10^{-5}$, and $\tan\alpha = 0.1$. We will show below, using the numerical model, that these differences are small given a very strong dependence of the flow on the aspect ratio when $L/H_0 < 2$.

5.3. *Regime transitions in the quasi-geostrophic model*

In figure 11 we show the flow regime transitions given by the quasi-geostrophic model, with the regime boundaries seen in the laboratory marked by grey lines for comparison. For the laboratory aspect ratio the regime boundaries (figure 11*a*) were in good agreement with the laboratory results for the transitions from quasi-linear to nonlinear stable flow and thence to periodic eddy shedding. The transition to nonlinear flow is shown by two dashed lines, corresponding to the two different criteria used to define separation: the radial vorticity gradient changed sign at the wall above the lower line, and recirculation at the wall (diagnosed by a change of sign of the vorticity at the wall) occurred above the upper line. Thus the region between the dotted lines corresponds to separation without recirculation. The transition to nonlinear flow found in the laboratory lies within this transition region. The transition to periodic eddy shedding occurred for Re_γ in the range 106–126, with a weak dependence on E. This transition occurs at slightly lower Re_γ than in the laboratory, probably because sustained periodic oscillation of the total kinetic energy was used instead of eddy shedding as the criterion for identifying flows in the unstable regime.

Under very strong forcing the total kinetic energy of the flow in the quasi-geostrophic model showed period-doubling behaviour, suggesting that this system becomes aperiodic through a period-doubling cascade. Another feature characteristic of the period-doubling route to chaos is the periodic 'window' in an otherwise aperiodic regime, at $E = 6.27 \times 10^{-5}$ and $Re_\gamma = 203$. The details of the transition to chaos are currently under further investigation. In the aperiodic regime the Fourier spectrum of the total kinetic energy shows a broad spectrum with no well-defined peaks, which is characteristic of chaos. The transition to chaos appears to be quite different from that seen in the laboratory, with the onset of aperiodicity dependent on E taking place at significantly smaller Re_γ than in the laboratory when E is small. This difference may reflect either the limitations of the quasi-geostrophic formulation

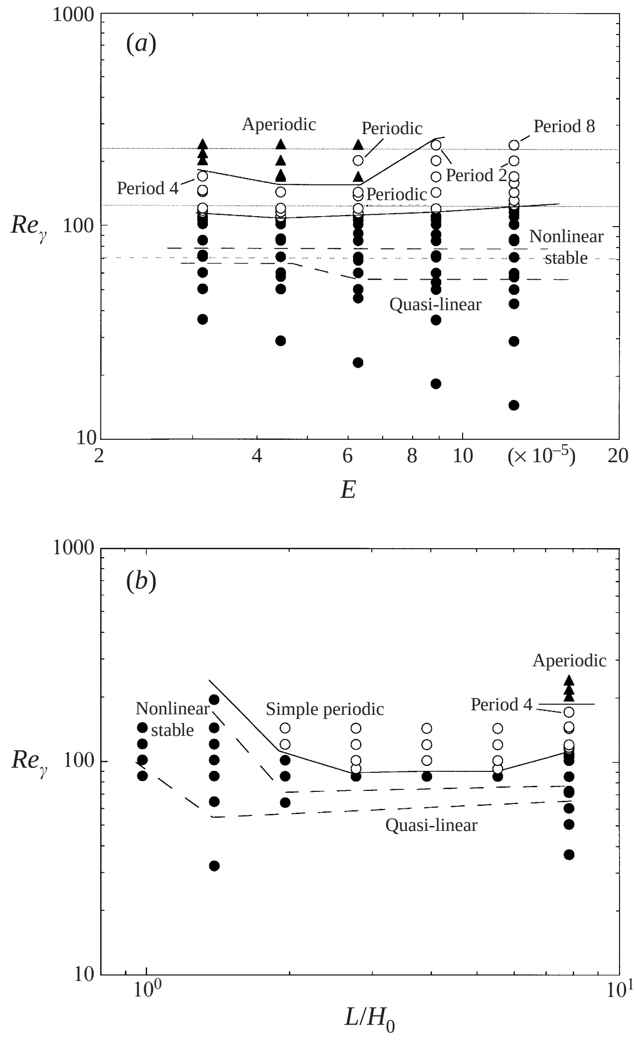

FIGURE 11. Flow regimes identified in the quasi-geostrophic numerical model. Transitions from stable (●) to unstable flow with periodic eddy shedding (○) and thence to aperiodic (▲) eddy shedding can be seen. (*a*) Regimes in Reynolds number–Ekman number space corresponding to the experimental results on figure 10 (the grey lines show for comparison the transitions found in the laboratory); (*b*) regime transitions in Reynolds number as a function of aspect ratio L/H_0 for basins of a fixed depth H_0, a fixed Ekman number $E = 3.14 \times 10^{-5}$ and bottom slope $\tan\alpha = 0.1$.

or numerical instability in the code (the numerical instability discussed by Leonard 1984 is largest when E is small and the forcing is strong).

The role of aspect ratio becomes clear when we plot the numerical model regimes in Reynolds number against L/H_0 (figure 11*b*) for fixed E, H_0 and $\tan\alpha$ (and thus the same value of $\beta = 2\Omega\tan\alpha/H_0$). The critical Reynolds number passes through a minimum at $L/H_0 \approx 2.5$. For wider basins it increases slowly. For narrow basins the flow is strongly stabilized by effects of the sidewalls, to the extent that we find no instability for $L/H_0 \leqslant 1.39$ (at the chosen values of E and $\tan\alpha$) even with very strong forcing. Streamfunctions for corresponding cases having a range of basin widths are

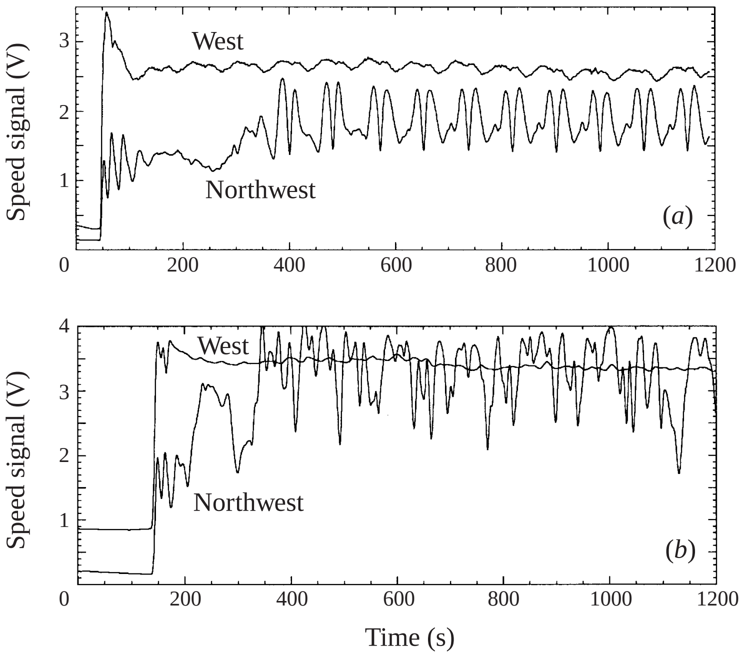

FIGURE 12. Records of voltage versus time from the thermistor speed probes for two runs in (*a*) the periodic regime ($Ro = 0.038$, $E = 3.15 \times 10^{-5}$, $\tan\alpha = 0.15$, $Re_\gamma = 160$) and (*b*) the aperiodic flow regime ($Ro = 0.077$, $E = 3.15 \times 10^{-5}$, $\tan\alpha = 0.15$, $Re_\gamma = 320$). Probes were positioned in the boundary current 3 cm from the west wall (upper trace, smaller signal variability) and in the region of eddy formation ($r = 30$ cm, $\theta = 27°$ west of 'north') (lower trace, larger signal variability). Only a short section of the record is reproduced here, including the initial transient after the lid forcing commences. The inertial period is 1.707 s.

shown in figure 4. A larger bottom slope, as in Beardsley (1973), is required to produce instability when L/H_0 is small.

5.4. *Regime transitions from fixed-point thermistor records*

As a complement to the classification of flow regimes based on flow visualization, a number of runs in the unstable regime were independently classified as periodic or aperiodic using characteristics of the time records from the thermistor devices. In all cases these classifications were found to be identical to those based on the flow visualization. Examples of thermistor records from two runs are shown in figure 12. As in all runs, the water was first brought to solid-body rotation before the lid forcing was begun. The record during the initial spin-up from rest after the forcing was turned on is an additional aspect of interest since it reveals at least two time scales of spin-up. There was a rapid development of the western boundary current within a few inertial periods (which corresponds to a few travel times T_R for topographic Rossby waves crossing the basin with a westward group speed c, where $T_R = L/c \sim \pi^2 H_0/(2\Omega L \tan\alpha \approx 4.1\,\mathrm{s})$. This was followed by a much slower spin-up of the mean flow in the boundary current over a time of order 60 inertial periods, and involving the initiation of eddy shedding. There appeared to be an even longer period (of order 200 inertial periods from the onset of forcing) before the unstable flow had adjusted towards its final state, either periodic or aperiodic. These transients are the subject of further investigation.

5.5. *Oscillation frequencies*

We used time-lapse video footage to measure the period of oscillations in the laboratory experiments within both the stable and periodic unstable regimes (figure 13). The periods ranged from 50 table rotation periods (100 inertial periods) under the weakest forcing to 4 rotation periods close to the transition to aperiodic flow. However, the modulation of oscillations by the lid rotation (via an unknown mechanism) was strong enough to force an integer number of cycles, n, within each lid period. Hence we first plot n as a function of the forcing strength Ro (figure 13*a*). For stable flows the relation between the two is not clear, whereas for unstable cases there is an approximate underlying trend $n \sim Ro^{-1}$. Alternatively, a plot of the oscillation period T_0 normalized by the rotation period T_Ω reveals a clear trend $T_0 \sim Ro^{-1}$ for the stable regime. The periods in stable cases collapse even more closely to a simple power-law curve when plotted against the Reynolds number Re_γ (figure 13*b*). The best fit, neglecting three scattered data points for stable cases close to the onset of instability, is $T_0/T_\Omega \approx 2.8 \times 10^3 Re_\gamma^{-4/3}$ for $Re_\gamma < 100$. On this same plot the periods measured for unstable runs ($Re_\gamma > 123$) remain widely scattered and consistently lie 50% to 100% above the trend of the stable oscillations. A similar change in behaviour between the two regimes is found if the periods are plotted against Ro (though in Ro there is some overlap of stable and unstable cases at $Ro \approx 0.3$–0.5). Some of the scatter for the unstable oscillations in figure 13(*b*) can be attributed to different Ekman numbers, and a plot of the periods against Ro/E shifts much of the data for unstable periods on to a single line (while producing large scatter in the data for stable cases). However, we are not able to find a functional form for the dependence on E that collapses all of the unstable periods onto a single curve.

In contrast to the laboratory results, the computed flow converged to a steady state in the stable regimes. Sustained periodic oscillations occurred only under conditions very close to the onset of eddy shedding. As conditions approached those giving sustained oscillations, the solution took an increasingly long time to converge to a steady state, displaying slowly decaying periodic oscillations in total kinetic energy. These decaying transients had a well-defined period of around 15–30 tank rotation periods. The period merged smoothly with the oscillation period in the periodic regime as the Reynolds number was increased past the onset of instability, suggesting that the transition to periodic flow is a supercritical Hopf bifurcation. The computed flow also showed fluctuations in total kinetic energy during its initial adjustment following the commencement of forcing. These fluctuations were not periodic, but had a dominant period of around 5–15 tank rotation periods, again with no detectable dependence on Rossby or Ekman number. The nature of these initial fluctuations has not been fully established, as they are significantly shorter than the shortest Rossby basin mode period of 37.8 tank rotation periods.

The characteristic timescales of the initial fluctuations and later decaying oscillations in the numerical model are similar to the period of stable oscillations observed in the laboratory close to the onset of instability, but are significantly shorter than the periods (of up to 50 days) observed at lower Rossby number. This disparity, and the independence of these timescales of E and Ro suggest that the lid period exerts a modulating effect on the amplitude of the stable oscillations seen in the laboratory, forcing a much longer modulation period at small Ro than the natural adjustment timescale would imply (though we recall that the observed oscillation period is only a fraction of the lid modulation period). If this conclusion is correct, then oscillations in the stable flow seen in the laboratory are a result of the system's extreme sensitivity

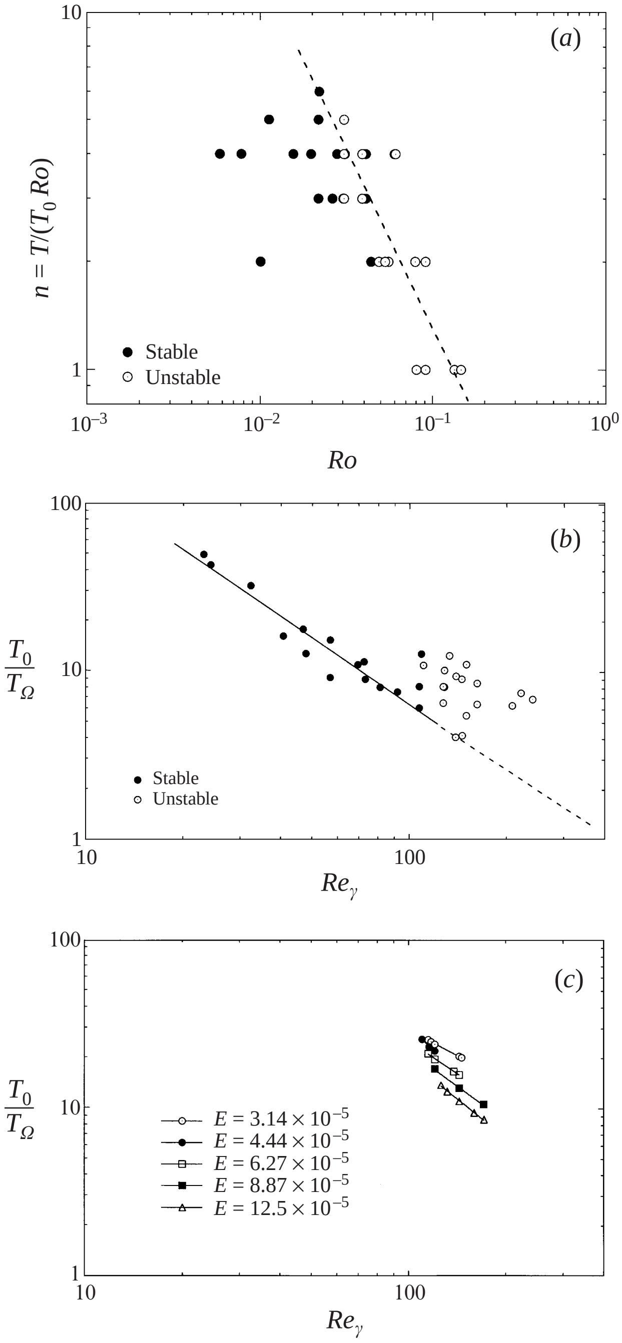

FIGURE 13. Period of oscillation or eddy shedding with anticyclonic forcing. (*a*) The number n of oscillations per lid rotation period in experiments ($n = 2\pi/(Ro\Omega T_0)$) as function of Rossby number; (*b*) the measured period expressed in rotation periods $2\pi/\Omega$ and plotted against the viscous boundary layer Reynolds number; (*c*) the period of total kinetic energy oscillations for periodic flows obtained from the numerical model, plotted as a function of the Reynolds number Re_γ for several values of the Ekman number, with $\tan\alpha = 0.1$. Period doubled, quadrupled and octupled points are not shown.

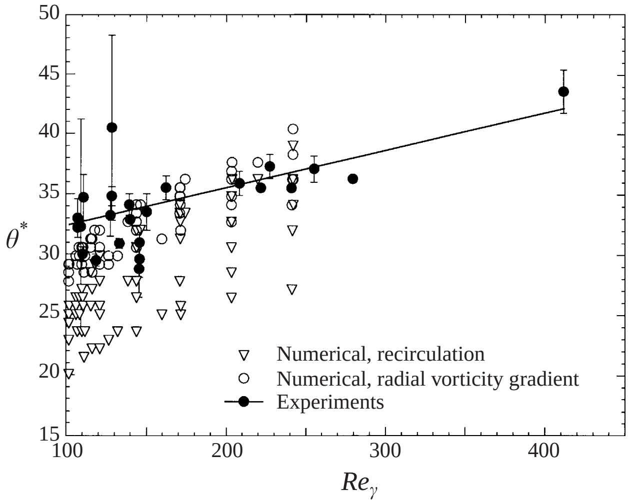

FIGURE 14. Separation position of the western boundary current (in degrees west of the shallowest point, 'north') as a function of the Reynolds number Re_γ in laboratory experiments and numerical results with anticyclonic forcing. Data are shown only for runs having $Re_\gamma > 100$. The best fit to the laboratory data is given by (25).

to very weak forcing. As noted previously, the mechanism responsible for the weak oscillations in the stable regime appears to be unrelated to the shear instabilities found above the critical forcing level, and is not expected to influence the locations of the regime transitions. We therefore find good agreement between transitions in the laboratory and numerical models.

On figure 13(*c*) we plot the period of the total kinetic energy $-\iint \psi\zeta \,\mathrm{d}x\,\mathrm{d}y$ against Re_γ for numerical solutions in the periodic, unstable regime (the model does not sustain continued oscillations in the stable regime). Points with doubled periods or aperiodic behaviour (see figure 11*a*) are not shown. The normalized period decreases approximately as Ro^{-1}, with the periods for different E falling on nearly the same line as a function of Ro (in contrast to the laboratory eddy-shedding periods which depended on Ro/E).

We conclude that the normalized period of stable, small-amplitude oscillations varied in a systematic fashion with Ro or Re_γ, whereas the large-amplitude oscillations and eddy shedding in unstable flows had normalized periods that varied approximately as Ro^{-1} and decreased with increasing Ekman number until the forcing was sufficient to lead to more complex eddy–eddy interactions. The latter results are contrary to previous interpretations of laboratory data (Beardsley 1969), which suggested that the period of eddy shedding was independent of Ro. We attribute the shorter normalized periods at greater lid speeds to a strong influence of the advection of disturbances along the boundary current. Also, the current, separated jet and eddies are wider for larger E, thus favouring longer length scales, which, for a given Ro, give larger normalized eddy-shedding periods.

6. Boundary current separation

The position of separation of the boundary jet in the homogeneous flow is of particular interest for later comparison with two-layer density-stratified flows. In the experiments separation was clearly defined only under conditions for which the current left the wall as a narrow jet. Its position, plotted as a function of Reynolds number in figure 14, was estimated from the path of a dyed streamline injected as close as possible to the wall without it entering the upflow in the viscous boundary layer. After passing through the jet and the circulation in the northeast of the basin some of the dye also entered a region of reversed flow in the northwest, north of the separation point, and the resulting confluence of the velocities parallel to the wall further confirmed the separation positions. Separation occurred at a mean azimuthal angle $\theta^* = 34.7^\circ \pm 3^\circ$ west of the shallowest point in the tank. It was insensitive to conditions, showing only a small shift toward the upstream direction (southward) for larger forcing:

$$\theta^* = 28.9 + 0.032 Re_\gamma. \tag{25}$$

Thus inertial overshoot of the current, which might be expected to give rise to a shift in the opposite direction (downstream) under strong forcing, was either not present or else was essentially independent of Rossby number throughout the unstable regime.

We used two criteria to objectively define the onset of position of boundary current separation in the numerical results: a change in sign of the vorticity at the boundary (indicating a region of reversed flow along the boundary) and a change in sign of the radial derivative of the vorticity at the boundary (indicative of a region of high vorticity extending into the interior). It was found that the latter criterion was the weaker definition, as it always occurred at lower Rossby number than that required to produce reversed flow. This results in a regime (between the dashed lines in figure 11*a*) in which there was separation without recirculation (as discussed in Becker & Page 1990). In cases when both criteria were satisfied, the change in sign of the radial vorticity gradient occurred about 1°–8° upstream of the change in sign of vorticity when $L/H_0 = 7.84$, with the difference tending to increase with increasing E. The difference also increased with decreasing L/H_0 (keeping H_0, E and $\tan\alpha$ fixed), reaching around 22° for $L/H_0 = 1.96$.

The position of separation in the quasi-geostrophic results is shown in figure 14. Separation occurred between 17° and 39° west of north (using the onset of recirculation to locate the separation point) or between 25° and 40° (using the change in sign of the radial vorticity gradient at the boundary). Although separation in the laboratory experiments was identified by recirculation, the numerical results agree best when the radial vorticity gradient criterion was used. This indicates that separation is slightly delayed in the numerical results, which may be related to the absence of an eastern boundary current.

The quasi-geostrophic model allowed a more detailed investigation of the separation process in terms of the higher-order pressure gradient (HOPG), that is, the part of the pressure gradient force which is not geostrophically balanced (Cessi 1991; Haidvogel *et al.* 1992). The part of the Coriolis term in the momentum equation (1) due to the horizontally non-divergent velocity can be written as the gradient of a scalar, and therefore can be entirely cancelled by the pressure gradient force. Any surplus ('higher order') pressure gradient is balanced by the remaining terms in the momentum equation. The higher-order pressure gradient is therefore given by

$$-\nabla p' = \frac{\partial \boldsymbol{u}}{\partial t} + Ro(\boldsymbol{u}\cdot\nabla)\boldsymbol{u} + 2\boldsymbol{k}\times\nabla_H\phi - E\nabla^2\boldsymbol{u}, \tag{26}$$

where ϕ is the scalar potential of the horizontally divergent velocity (estimated by solving (10), neglecting the contribution of the horizontally divergent velocity to the orographic term). Since $\nabla p'$ is irrotational, it is actually balanced only by the divergent part of the inertial term, since the other terms in the right-hand side of (26) are non-divergent due to incompressibility (these terms serve only to cancel the non-divergent part of the inertial term).

The horizontal part of (26), which we will call the HOPG, was calculated from the quasi-geostrophic results for flow regimes ranging from quasi-linear to periodic eddy shedding. It was found that the HOPG acted to accelerate the flow into the western boundary current in the southwest. This favourable HOPG persisted across the width of the southern part of the boundary current for all Rossby numbers investigated. Further to the north the outer parts of the boundary current began to decelerate under the influence of an adverse HOPG, while the flow against the wall remained in a region of favourable HOPG. In the quasi-linear regime the HOPG was favourable nearly everywhere against the boundary, although it could be very weakly adverse at the extreme northern end of the boundary current under conditions close to the onset of separation. The transition to strongly nonlinear flow coincided with the penetration of a region of significantly adverse HOPG to the sidewall. When the adverse HOPG at the sidewall was relatively weak and present along only a short section of the sidewall, it was insufficient to create reversed flow along the wall, and the flow separated without recirculation. The separation of the outer part of the boundary layer was due to the much stronger adverse HOPG experienced over a much longer streamline path. Stronger forcing increased both the size and the strength of the region of adverse HOPG along the wall until it was sufficient to reverse the flow along the wall and recirculation was observed. Thus the adverse HOPG seems to offer a good explanation of western boundary current separation in this model, consistent with the earlier conclusion of Cessi (1991).

The laboratory experiments displayed a small ($\pm 3^\circ$) fluctuation in the separation position associated with the eddy shedding frequency, recalling that eddy shedding was coupled to fluctuations in the western boundary current via Rossby waves that permeated the entire basin. Corresponding fluctuations in the current speed at the west, measured 2 cm from the wall, can be seen in the thermistor speed probe records in figure 12. Dye streams revealed the advection of these fluctuations along the current from the west to the eddy-shedding region. Within the current the disturbances were recognized as variations in the radial position of each dyed stream. The fluctuations, coupled with large horizontal velocity gradients within the boundary current, sometimes led to the development of sharp folds or kinks in the passive tracer streams and these could be followed to the eddy shedding region.

7. Conclusions

Both the numerical model and the experiments have revealed transitions from approximately quasi-linear flow to nonlinear stable flow and to an unstable periodic regime. The experiments have revealed a further transition to aperiodic or chaotic flow, which appears to be related to increased eddy–eddy and eddy–jet interactions. This latter transition was not reliably reproduced by the quasi-geostrophic model.

Of the various Reynolds numbers available Re_γ is the most useful for interpreting the observed transitions. This Reynolds number, based on the width and velocity scales of the $E^{1/3}$-boundary layer, is also more physically plausible as a governing parameter for the flow than was the previously suggested 'Ekman-layer Reynolds number' based on the Ekman pumping velocity. The observation that the transition to unstable eddy-shedding flow occurs at a fixed value of Re_γ is evidence that the eddy-shedding instability is a shear instability of the separated jet, as suggested by Becker & Page (1990). Significantly, the flow visualization showed clearly that unsteadiness of the jet in the region where it makes a rapid adjustment to join the slow interior flow propagates back through the interior into the upstream regions of the boundary current. From there the fluctuations were seen to be advected with the current and provide a positive feedback to the unsteady adjustment and eddy shedding. The numerical results suggest that the onset of instability occurs through a supercritical Hopf bifurcation.

The quasi-geostrophic model showed the crucial influence of basin aspect ratio on flow behaviour. In particular, it was revealed that the relatively deep sliced cylinders used in previous work (Beardsley 1969, 1973; Beardsley & Robbins 1975; Becker & Page 1990) resulted in significant stabilization of the flow, since the western boundary current occupied a large proportion of the basin width and was therefore strongly constrained by the lateral boundaries.

The measurements of velocities and transports in the laboratory and numerical flows (as functions of the Rossby and Ekman numbers and the bottom slope) were generally consistent with each other, and also in good agreement with linear theory when $Ro < E^{1/2}$. The quasi-geostrophic model shows that western boundary current separation in the sliced cylinder is due an adverse higher-order pressure gradient. The distribution of this pressure gradient explains the separation without recirculation observed under some conditions.

The authors would like to thank an anonymous reviewer for helpful suggestions regarding the formulation used in the numerical model.

REFERENCES

Beardsley, R. C. 1969 A laboratory model of the wind-driven ocean circulation. *J. Fluid Mech.* **38**, 255–271.

Beardsley, R. C. 1972 A numerical investigation of a laboratory analogy of the wind-driven ocean circulation. *NAS Symp. on Numerical Models of Ocean Circulation*, p. 311.

Beardsley, R. C. 1973 A numerical model of the wind-driven ocean circulation in a circular basin. *Geophys. Fluid Dyn.* **4**, 211.

Beardsley, R. C. 1975 The 'sliced-cylinder' laboratory model of the wind-driven ocean circulation. Part 2. Oscillatory forcing and Rossby wave resonance. *J. Fluid Mech.* **69**, 41–64.

Beardsley, R. C. & Robbins, K. 1975 The 'sliced-cylinder' laboratory model of the wind-driven ocean circulation. Part 1. Steady forcing and topographic Rossby wave instability. *J. Fluid Mech.* **69**, 27–40.

Becker, A. & Page, M. A. 1990 Flow separation and unsteadiness in a rotating sliced cylinder. *Geophys. Astrophys. Fluid Dyn.* **55**, 89–115.

Bennetts, D. A. & Hocking, L. M. 1973 On nonlinear Ekman and Stewartson layers in a rotating fluid. *Proc. R. Soc. Lond.* A **333**, 469–489.

Böning, C. W. 1986 On the influence of frictional parameterization in wind-driven ocean circulation models. *Dyn. Atmos. Oceans* **10**, 63–92.

Bryan, K. 1963 A numerical investigation of a nonlinear model of a wind-driven ocean. *J. Atmos. Sci.* **20**, 594–606.

Cessi, P. 1991 Laminar separation of colliding western boundary currents. *J. Mar. Res.* **49**, 697–717.

Dengg, J. 1993 The problem of Gulf Stream separation: a barotropic approach. *J. Phys. Oceanogr.* **23**, 2182–2200.

Greenspan, H. P. 1969 A note on the laboratory simulation of planetary flows. *Stud. Appl. Maths* **48**, 147–152.

Griffiths, R. W. & Cornillon, P. 1994 Laboratory experiments with mid-latitude circulation in a two-layer ocean. *4th Intl Symp. on Stratified Flows, Grenoble, France* (ed. E. Hopfinger, B. Voisin & G. Chavand). Institute de Mécanique de Grenoble.

Griffiths, R. W. & Veronis, G. 1997 A laboratory study of the effects of a sloping side boundary on wind-driven circulation in a homogeneous ocean model. *J. Mar. Res.* **55**, 1103–1126.

Griffiths, R. W. & Veronis, G. 1998 Linear theory of the effect of a sloping side boundary on circulation in a homogeneous laboratory model. *J. Mar. Res.* **56**, 75–86.

Haidvogel, D. B., McWilliams, J. C. & Gent, P. R. 1992 Boundary current separation in a quasigeostrophic, eddy-resolving ocean circulation model. *J. Phys. Oceanogr.* **22**, 882–902.

Ierley, G. R. 1990 Boundary layers in the general ocean circulation. *Ann. Rev. Fluid Mech.* **22**, 111–142.

Ierley, G. R. & Young, W. R. 1991 Viscous instabilities in the western boundary layer. *J. Phys. Oceanogr.* **21**, 1323–1332.

Israeli, M. 1970 A fast implicit numerical method for time dependent viscous flows. *Stud. Appl. Maths* **49**, 327–349.

Kamenkovitch, V. M., Sheremet, V. A., Pastushkov, A. R. & Belotserkovsky, S. O. 1995 Analysis of the barotropic subtropical gyre in the ocean for finite Reynolds numbers. Part I. *J. Mar. Res.* **53**, 959–994.

Leonard, B. P. 1984 Third-order upwinding as a rational basis for computational fluid dynamics. In *Computational Techniques and Applications: CTAC-83* (ed. J. Noye & C. Fletcher). Elsevier.

Meacham, S. P. & Berloff, P. S. 1997 Barotropic, wind-driven circulation in a small basin. *J. Mar. Res.* **55**, 523–563.

Munk, W. H. 1950 On the wind-driven ocean circulation *J. Met.* **7**, 79–93.

Munk, W. H. & Carrier, G. F. 1950 The wind-driven circulation in ocean basins of various shapes. *Tellus* **2**, 158.

Page, M. A. 1981 Rotating fluids at low Rossby number. PhD thesis, University College, London.

Page, M. A. 1982 A numerical study of detached shear layers in a rotating sliced cylinder. *Geophys. Astrophys. Fluid Dyn.* **22**, 51–69.

Parsons, A. T. 1969 A two-layer model of Gulf Stream separation. *J. Fluid Mech.* **39**, 511–528.

Pearson, C. E. 1965 A computational method for viscous flow problems. *J. Fluid Mech.* **21**, 611–622.

Pedlosky, J. 1979 *Geophysical Fluid Dynamics*. Springer.

Pedlosky, J. 1987 On Parson's model of the ocean circulation. *J. Phys. Oceanogr.* **17**, 1571–1582.

Pedlosky, J. & Greenspan, H. P. 1967 A simple laboratory model for the oceanic circulation. *J. Fluid Mech.* **27**, 291–304.

Sheremet, V. A., Kamenkovitch, V. M. & Pastushkov, A. R. 1995 Analysis of the barotropic model of the subtropical gyre in the ocean for finite Reynolds numbers. Part II. *J. Mar. Res.* **53**, 995–1024.

Stommel, H. 1948 The westward intensification of wind-driven ocean currents. *Trans. Am. Geophys. Union* **29**, 202.

Veronis, G. 1973 Model of world ocean circulation: I. wind-driven, two-layer. *J. Mar. Res.* **31**, 228–288.

Verron, J. & Le Provost, C. 1991 Response of eddy-resolving general circulation numerical models to asymmetrical wind forcing. *Dyn. Atmos. Oceans* **15**, 505–534.